Influence of the Saharan Air Layer on Hurricane Nadine (2012). Part I: Observations from the Hurricane and Severe Storm Sentinel (HS3) Investigation and Modeling Results

Jainn J. Shi[1,2], Scott A. Braun[1], Zhining Tao[1,3], and Toshihisa Matsui[1,4]

1. NASA/Goddard Space Flight Center
2. Morgan State University, Baltimore, Maryland
3. Universities Space Research Association, Columbia, Maryland
4. *Earth System Science Interdisciplinary Center, University of Maryland, College Park, Maryland*

Submitted to Monthly Weather Review

Oct. 23, 2020

Corresponding author: Dr. Jainn J. Shi, Morgan State University, Baltimore, MD 21251.
jainn.j.shi@nasa.gov

Abstract

This study uses a model with aerosol-cloud-radiation coupling to examine the impact of Saharan dust and other aerosols on Hurricane Nadine (2012). In order to study aerosol direct (radiation) and indirect (cloud microphysics) effects from individual, as well as all aerosol species, eight different NU-WRF simulations were conducted. In several simulations, aerosols led to storm strengthening, followed by weakening relative to the *Ctrl* simulation. This variability of the aerosol impact may be related to whether aerosols are ingested into clouds within the outer rainbands or the eyewall. Upper tropospheric aerosol concentrations indicate vertical transport of all aerosol types in the outer bands but only vertical transport of sea salt in the inner core. The results suggest that aerosols, particularly sea salt, may have contributed to a stronger initial intensification, but that aerosols ingestion into the outer bands at later times may have weakened the storm in the longer term. In most aerosol experiments, aerosols led to a reduction in cloud and precipitation hydrometeors, the exception being the dust-only case that produced periods of enhanced hydrometeor growth. The Saharan Air Layer (SAL) also impacted Nadine by causing a region of strong easterlies impinging on the eastern side of the storm. At the leading edge of these easterlies, cool and dry air near the top of the SAL was being ingested into the outer-band convection. This midlevel low equivalent-potential-temperature air gradually lowered toward the surface and eventually contributed to significant cold pool activity in the eastern rain band and in the northeast quadrant of the storm. Such enhanced downdraft activity could have led to weakening of the storm, but it is not presently possible to quantify this impact.

1. Introduction

The impact of the Saharan air layer (SAL) on the development and intensification of hurricanes has garnered significant attention in recent years. The SAL is formed by strong surface radiative heating over the Saharan desert, which results in a deep well-mixed layer with warm temperatures and low relative humidity in the lower troposphere. When the warm and dry air of the SAL moves off the western African coast, it is elevated over the cooler, moister marine boundary layer (Carlson and Prospero 1972; Prospero and Carlson 1981; Karyampudi and Carlson 1988). Past studies yielded mixed results in terms of the impact of the SAL on hurricanes (Karyampudi and Carlson 1988; Karyampudi et al. 1999; Karyampudi and Pierce 2002; Dunion and Velden 2004; Braun 2010; among others mentioned below). Karyampudi and Carlson (1988) and Karyampudi and Pierce (2002) suggested that the SAL contributes to African easterly wave (AEW) growth and, in some cases tropical cyclogenesis, by supporting convection along its leading and southern borders. Karyampudi and Carlson (1988) suggested that SAL can fuel AEW growth and assist the development of tropical cyclones from AEW disturbances during initial stages of development. Jones et al. (2004), using 22 years of analysis increments of geopotential height from National Centers for Environmental Prediction—National Centers for Atmospheric Research (NCEP—NCAR) reanalysis data and information on dust from a global transport model, found larger amplitudes in the analysis than in the first guess, suggesting amplification of AEWs due to the radiative effects of dust.

On the other hand, Dunion and Velden (2004) discussed mechanisms that usually hinder the genesis and intensification of tropical cyclones. They suggested that the SAL negatively impacts tropical cyclones through: 1) vertical wind shear resulting from an increase of low-level easterlies in the African easterly jet (AEJ); 2) cold downdrafts enhanced by the intrusion of dry

SAL air into tropical cyclones; and 3) a temperature inversion in the lower troposphere enhanced by the radiative warming of dust that results in suppression of deep convection. Lau and Kim (2007a, 2007b) and Sun et al. (2008) speculated that dry air or dustiness from increased SAL activity was the cause of reduced Atlantic hurricane activity in 2006 and 2007 as compared to 2004 and 2005. Wu (2007) linked the increase of Atlantic hurricane activity to a decrease in SAL activity and enhanced vertical wind shear associated with dusty and dry air outbreaks.

Braun (2010) suggested that, after storm genesis, the SAL does not have a statistically significant impact on the subsequent intensification. Another interpretation of Braun's (2010) findings is that the SAL can have both positive and negative impacts that lead to an inconsistent response that cancels in a statistical analysis. Braun et al. (2013) used a suite of satellite data, global meteorological analyses, and airborne data to conclude that the impact of the SAL on Helene was confined to the earliest stages of development. Dry air observed to wrap around Helene was determined to be of non-Saharan origin and appeared to have little impact on storm intensity.

Saharan dust can affect storms in a couple different ways. First, dust can modify cloud microphysical processes within the storm by providing cloud condensation and ice nuclei (Khain et al. 2008, 2010). Second, the dust can absorb incoming solar radiation, which warms the dust layer (Carlson and Benjamin 1980) and reduces the solar radiation that reaches the surface (Lau and Kim 2007b; Reale et al. 2009). Chen et al (2010), using aerosol-radiation coupling in WRF, revealed that the dust-radiation interaction mainly warmed the dust layer between 750 and 550 hPa, which resulted in increased vertical wind shear by about 1-2.5 m s^{-1} km^{-1} to the south of the SAL, where AEW disturbances and tropical storms usually occur. Their results were rather inconclusive about the actual impact of dust-radiation interactions on tropical cyclone genesis and intensity change, and were hindered by the lack of aerosol-microphysics interactions. Changes in moisture and temperature distributions as a result of dust-radiation interactions could also impact cloud processes.

It is well known that aerosols in the atmosphere often serve as cloud condensation nuclei (CCN) and ice nuclei (IN) in the formation of cloud droplets and ice particles, respectively. As a result, these aerosols exert considerable influence on the microphysical properties of both liquid and ice clouds and have been proposed to impact tropical cyclone intensity (Cotton et al. 2007, 2012; Zhang et al. 2007 and 2009; Khain et al. 2010; Rosenfeld et al. 2011, 2012; Tao et al. 2012; Herbener et al. 2014). Cotton et al. (2007) and Khain et al. (2010) suggested that hurricane intensity might be reduced if the intrusion of large concentrations of small hygroscopic particles (such as from pollution) occurs during storm development. However, for dust particles that often serve as sources of giant CCN or IN, the impact is non-monotonic and can lead to either decreases (Zhang et al. 2007 and, 2009) or increases (Herbener et al. 2014) in storm intensity. Many of these studies were highly idealized, in some cases (Zhang et al. 2007 and 2009) with unrealistic horizontally uniform dust fields surrounding and within the storms. A more realistic distribution of aerosols, still in an idealized setting, with dust advected into the storm, may partially account for the finding of strengthening storms in Herbener et al. (2014). However, more realistic prescriptions of storm environments and dust distributions are needed to better evaluate the impact of Saharan dust on tropical cyclones. Radiative and microphysical impacts of aerosol on weather systems, especially in numerical models, are usually considered separately. Rosenfeld et al. (2008) emphasized that these two effects need to be studied together due to the opposing microphysical and radiative effects that aerosols have on deep convective clouds. Shi et al. (2014) examined the combined effects of SAL dust on a mesoscale convective system over Africa and showed that the onset of precipitation was delayed about 2 hours due to aerosol-radiation-cloud microphysics effects.

The National Aeronautics and Space Administration's (NASA) Hurricane and Severe Storm Sentinel (HS3) investigation was a multi-year field campaign designed to improve understanding of the physical processes that control hurricane formation and intensity change, specifically the relative roles of environmental and inner-core processes (Braun et al. 2016, hereafter B16). Funded as part of NASA's Earth Venture program, HS3 conducted five-week campaigns during the hurricane seasons of 2012-14 using the NASA unmanned Global Hawk aircraft. In September 2012, HS3 flew five missions into Hurricane Nadine, the first two of which involved the interaction of Nadine with the SAL. As reported by B16, Nadine was HS3's best case for examining the interaction of a tropical cyclone with the SAL. They speculated that the dry SAL air was on the downshear side of the storm and the storm inflow may have provided a pathway for the SAL dry air and dust to get into the inner-core circulation. They concluded that it was not possible to determine the impact of the SAL dust from the HS3 observations alone.

Since the HS3 observational data alone can't be used to determine the impact of the SAL dust on Nadine, this study utilizes a complete modeling system with an inline aerosol distribution forecast to study the possible impact of dust from the SAL and other aerosol sources on Hurricane Nadine. The modeling system is the NASA Unified Weather Research and Forecast (NU-WRF) model. A brief history of Hurricane Nadine and description of HS3 observations of the storm are given in Section 2. Details of the NU-WRF model and simulation setup are given in section 3. In section 4, results from the control simulation are compared with HS3 in-situ and remote sensing and satellite observations. Discussion and conclusions are given in Section 5.

2. Hurricane Nadine (2012) and Observations from HS3

a. History of Nadine

Nadine was a long-lasting hurricane that meandered in the middle of the Atlantic Ocean for more than three weeks (10 September to 3 October, see the NHC best track on Fig. 1) (Brown 2013). Nadine started out as an organized vortex that formed from an AEW that moved offshore of the West African coast on 7 September, along with a significant plume of dust to its north (not shown). Over the next several days, a broad low pressure area developed in conjunction with the AEW as convective activity increased and became more organized, leading to the eventual formation of a tropical depression on 10 September.

The depression continued its west-northwestward movement to the south of a large subtropical ridge over the central and eastern Atlantic and was declared a tropical storm on 12 September. Then, Nadine turned northwestward and continued to strengthen when it moved into a low-shear environment and over warmer waters. Nadine started turning northward around 1200 UTC 13 September and became a hurricane by 1800 UTC 14 September. Nadine remained a hurricane during the next two days as it moved rapidly eastward around the northern side of the subtropical ridge under the influence of strong southwesterly to westerly shear. As Nadine turned east-northeastward early on 17 September, it decelerated and weakened. For the next 17 days, Nadine slowly meandered in the middle of the Atlantic before re-strengthening to a hurricane on 28 September. Nadine eventually dissipated on 4 October. This study focuses on the early part of Nadine's life span between 10 and 17 September.

Braun et al. (2016, their Fig. 8) showed that a SAL dust outbreak emerged from the West African coast immediately following the pre-Nadine disturbance. The dust outbreak moved westward over the next several days with its leading edge catching up to Nadine at the time of tropical depression formation. The dusty air mass gradually overtook Nadine, extending around the northwestern side of the storm by the time Nadine reached tropical storm strength, and then continued moving northwestward with the storm. Observations of Nadine and the SAL dust will be examined in the next section.

b. Nadine observations during HS3

Nadine became a tropical storm at 00 UTC 12 September, during the middle of the first HS3 Global Hawk flight, and a hurricane at 18 UTC 14 September, during the second HS3 flight (B16). In this section, we examine data collected during these two HS3 flights that highlight aspects of the storm not discussed by B16. As they mentioned, dropsonde data were collected in the western part of the storm during the 11-12 September flight, but were discontinued midway through the flight after a dropsonde became jammed in the launcher, so unfortunately there are no dropsonde data available in the SAL air mass to the east of the storm center. All data collected during the HS3 field campaign for Nadine including those analyzed for this study can be found at https://ghrc.nsstc.nasa.gov/home/projects/hs3.

Braun et al. (2016) showed a time series of data from the Cloud Physics Lidar (CPL) and Scanning High-resolution Interferometer Sounder (S-HIS) for the eastern segment of the flight (see their Fig. 9), showing an extensive dust layer approximately 5 km deep, with warm and dry air between 900 to 650 hPa. A similar time series (Fig. 2) for the western portion of the same flight (the first three north-south-oriented flight legs, indicated by red lines in our Fig. 9b) suggests an environment that was largely devoid of significant SAL air compared to the eastern side of the storm shown by Braun et al. (2016). Shallow aerosol layers were seen up to about 800-700 hPa between 1700-1800 UTC and 1940-2100 UTC 11 September when the aircraft moved beyond regions of high clouds associated with Nadine that had obscured views of lower levels. The first detectable aerosol layer (top near ~750 hPa) was at the southern end of the first flight leg moving from north to south, with no dust present at the north end and a shallow layer of aerosols at the southern end that was characterized by aerosol backscatter values less than about 0.03 km^{-1} sr^{-1} and relative humidities >70%; immediately above the aerosol layer, between 750-550 hPa, relative humidity was quite variable with alternating moist and dry areas. Temperature perturbations (derived by removing the average temperature from 2000 UTC 11 September to 0600 UTC 12 September) of ~0-3 K generally presided over the layer from 850-450 hPa. A representative dropsonde profile in this region, shown in Fig. 3 (red line), confirms the S-HIS data, with values generally above 75%, but as low as 65%, in the aerosol layer and drier air (<60%) not being observed except above 530 hPa.

Between 2020-2050 UTC 11 September, at the north end of the second flight leg after the aircraft moved northward of Nadine's high cloud cover, a second region of enhanced lidar aerosol backscatter was apparent in the lower troposphere (Fig. 2a), extending up to about 700 hPa. Coincident with this aerosol backscatter was a low-level layer of warmer temperature perturbations (~6-9 K), suggesting a narrow region of SAL air. A dropsonde profile at 2045 UTC is shown in Fig. 3 (black line) and indicates a temperature inversion between ~820-800 hPa and a layer from ~800-700 hPa in which the temperature was characterized by a steeper lapse rate just above the inversion (compared to the earlier dropsonde) and the vapor mixing ratio was approximately constant, indicative of a shallow, elevated residual SAL air mass. This dropsonde profile, taken due north of the storm center, was the only dropsonde obtained during the flight to clearly indicate SAL air, while others on the western side of the storm did not indicate the presence of SAL air (recall, no dropsondes were available east of this flight line). Combined with results on the eastern side of Nadine as seen in Figs. 8b and 9 of B16, the data suggest a SAL air mass that was rapidly encroaching on the eastern side of Nadine, but was only just beginning to wrap around the northern side during this flight.

On 13 September, MODIS (Moderate Resolution Imaging Spectroradiometer) indicated that dust was most concentrated in the northeastern quadrant of the storm (Fig. 8d of B16). A CALIPSO overpass near this region on the eastern side of Nadine and cutting through the SAL is shown as the black line in Fig. 4a. Similar to the CPL data on 11-12 September (Fig. 9 of B16), the dust layer extended upward to about 5 km altitude. High clouds associated with Nadine obscured part of the dust layer between 22-26°N (Fig. 4b). While the low-level air within the SAL is typically dry, clouds at the top of the dust layer near 28°N indicate the high relative humidity that can be found in the upper part of the SAL (Messager et al. 2010; Braun 2010). While dust dominates above the boundary layer, marine aerosols and dusty marine air are seen on the south side of the SAL dust and, to a lesser extent, to the north of the SAL.

The 14-15 September flight occurred as Nadine was moving northward near 54°W with the SAL air present on its eastern and northern sides (Fig 8e of B16). A CALIPSO overpass (not shown) along the western side of Nadine between 55-60°W indicated mostly marine or dusty marine air below 2 km (~800 hPa) altitude. Dropsonde data covering the entire 14-15 September flight, with drop locations adjusted for storm motion to a reference time of 00 UTC 15 September, are shown in Figs. 5a-c. At 875 hPa (Figs. 5a-b), the region to the east and north of Nadine's outer rainband was dry and warm relative to other sectors of the storm, with relative humidities generally below 50% in the SAL air, but greater than 70% elsewhere. Temperatures in the SAL at 875 hPa exceeded ~293 K, but were as low as 289-290 K elsewhere. Although the CALISPO retrieval indicated dusty marine aerosols up to about 800 hPa to the west of Nadine, the thermodynamic conditions within this layer were not indicative of SAL air.

Thermodynamic conditions changed markedly across the outer rainband to the southeast of the storm center, indicated by two dropsonde profiles in Fig. 5d (locations are indicated in Fig. 5b). To the east (black profile), the warm SAL air is apparent where its warm temperatures produce a strong inversion above the boundary layer. Near the top of the SAL, temperatures are cooler than the environment, producing a second inversion near 600 hPa (Karyampudi et al. 1999). In contrast, to the west of the outer rainband, a dropsonde profile (red line) shows relatively moist conditions up to 500 hPa, but very dry air aloft. Figure 5c shows that at 400 hPa very dry air was impinging on the western and northern sides of Nadine as strong vertical wind shear [~13 m s^{-1} between 850-200 hPa; B16] was inhibiting intensification above minimal hurricane status. Braun et al. (2016) hypothesized that the rainband located about 4-5° to the east and southeast of Nadine's center may have acted as a boundary between the SAL air mass and the non-SAL air predominant within the hurricane vortex, but could not determine the impact of the SAL from these observations.

The remainder of this paper uses numerical simulations of Nadine using NU-WRF, which includes the effects of aerosols, to examine the impact of Saharan dust and other aerosols on storm microphysical structure and intensity. Part II will use 30-member ensemble simulations with all aerosols, dust only, and no aerosols to further quantify the role of the SAL in this case.

3. Numerical Simulations of Hurricane Nadine

a. NASA Unified WRF (NU-WRF)

The NU-WRF modeling system is based on the Advanced Research WRF released by NCAR. The philosophy behind NU-WRF development is to provide a NASA-oriented version that incorporates a unique set of NASA tools related to physics, validation, and assimilation of current

Earth science satellite observations into the model (Shi et al. 2010, 2014; Peters-Lidard et al. 2015; Tao et al. 2017). NU-WRF was developed at NASA's Goddard Space Flight Center (GSFC), in collaboration with NASA's Marshall Space Flight Center (MSFC) and university partners, as an observation-driven integrated modeling system that represents aerosol, cloud, precipitation, and land processes at satellite-resolved scales (Peters-Lidard et al. 2015).

NU-WRF components used in this study include Version 3 of the ARW dynamical core (Skamarock et al. 2008), the WRF-Chem embedded version of the Goddard Chemistry Aerosols Radiation Transport model (GOCART; Chin et al. 2000a, 2000b), the GSFC radiation and microphysics schemes including revised couplings to aerosols (Tao et al. 2003; Lang et al. 2007, 2011; Shi et al. 2014; Matsui et al. 2018), and the Goddard Satellite Data Simulator Unit (G- SDSU; Matsui et al. 2013, 2014). Details about the NU-WRF modeling system and its availability can be found at https://nuwrf.gsfc.nasa.gov.

b. Aerosol-cloud microphysics-radiation coupling in NU-WRF

The Goddard microphysics and radiation schemes in NU-WRF have been coupled with the aerosol fields forecasted by GOCART in WRF-Chem to account for the aerosol direct (radiation) and indirect (cloud microphysics) effects. In the current coupling, all atmospheric parameters including aerosols and cloud and precipitation hydrometeor masses are explicitly predicted on the same high-resolution grid at every time step. In the Goddard one-moment microphysics scheme, both CCN and IN are diagnostic parameters activated from the aerosol mass concentrations of all 14 WRF-Chem/GOCART-predicted aerosol species. Following Shi et al. (2014), the activation of CCN is adapted from Koehler *et al.* (2006) and Andreae and Rosenfeld (2008) while IN is following Demott *et al.*(2010). Wet deposition is handled within the GOCART/WRF-Chem module with a simplified parameterization using the model forecast precipitation and is not handled explicitly by the cloud microphysics. The CCN are used to calculate the auto-conversion of cloud droplets to form rain to account for the aerosol impact on warm-rain processes based on Liu and Daum (2004). To account for the aerosol impact on ice processes, IN are used to parameterize the Bergeron process, which is the transfer rate of cloud ice to snow, and to parameterize the depositional growth of cloud ice at the expense of cloud water (Meyers et al., 1992; DeMott et al., 2010). Due to the relatively coarse 3-km grid spacing on the innermost mesh, the supersaturation conditions for activation of CCN is seldom met. As a result, the primary microphysical impact of the aerosols is as IN. In the Goddard longwave (LW) and shortwave (SW) radiation schemes (Chou and Suarez 1999, 2001; Matsui et al. 2018), all 14 GOCART aerosol species are used to calculate the aerosol optical thickness, single-scattering albedo, and asymmetry factor to estimate aerosol-induced radiative heating (Shi et al. 2014). The Goddard radiation scheme also accounts for the single scattering properties of snow, graupel, and rain (Matsui et al. 2018).

c. Model setup and simulation design

Doubly nested domains were constructed with a horizontal grid spacing of 27, 9, and 3 km with corresponding grid dimensions of 601×421, 802×655, and 832×931 points for the outer, middle, and inner domains, respectively (Fig. 6). The outer domain (D1) extends from just off the west coast of the U.S. continent to the eastern Saharan Desert. It is large enough to contain carbon pollution due to forest fires that started a few days earlier in the northwestern U.S., that will be carried eastward by upper-tropospheric westerlies (see the WRF AOD over the northwestern U.S. in Fig. 6, to be discussed in the next section) during the simulation, and the entire SAL dust outbreak that originates over North Africa. The inner domain (D3) is large enough to cover the vast area that Nadine traveled during the integration span in this study. This large inner (D3) domain was necessitated by the fact that WRF-Chem does not support moving nests. No further nest refinement that could cover the storm for more than a short time was possible. A terrain-following vertical coordinate with 61 layers was used with resolutions of 5~10 hPa inside the planetary boundary layer (PBL) and 20~25 hPa above the PBL. Time steps of 60, 20, and 6.66 s were used in the outer and two nested grids, respectively. The Grell–Devenyi ensemble cumulus parameterization scheme (Grell and Devenyi 2002) was used to account for large-scale precipitation processes. The PBL parameterization for this study was the the Yonsei University PBL scheme (Hong et al. 2006; Hong, 2007). The surface heat and moisture fluxes (from both ocean and land) were computed from similarity theory (Monin and Obukhov 1954). Land-surface sensible and latent heat fluxes are predicted by the Noah-land surface model (LSM, Chen and Dudhia 2001).

In this study, NU-WRF was initialized from the NCEP Global Forecast System (GFS) analyses with 1° grid resolution at 0000 UTC 10 September 2012. Time-varying lateral boundary conditions and soil temperature and moisture values for the NOAH-LSM at 6-hour intervals were also taken from the NCEP/GFS analyses. Because of its better representation of observations, sea surface temperature was taken from the ERA-Interim global reanalysis data (Dee et al., 2011) and updated daily. The model was integrated for 168 hours, from 00 UTC 10 September to 00 UTC 17 September 2012. For the GOCART part of WRF-Chem, the Goddard Earth Observing System Data Assimilation System (GEOS DAS, with output saved every 3 hours) was used for the initial and time-varying lateral boundary conditions (Chin et al. 2009). The coupled NU-WRF GOCART simulations were also driven by both anthropogenic and natural emissions, which were obtained from the emission database compiled for the global GOCART simulation (Chin et al. 2009). Details of how NU-WRF calculates the anthropogenic and natural emissions of sulfate, black carbon (BC), organic carbon (OC), dust and sea salt can be found in Shi et al (2014).

In order to study aerosol direct (radiation) and indirect (cloud microphysics) effects from individual as well as all aerosol species, eight different NU-WRF simulations (Table 1) were conducted including: 1) the control experiment with no aerosol coupling (Exp. Ctrl); 2) full aerosol effects included in the cloud microphysics but not in radiation (*AM*); 3) full aerosol effects in radiation but not in the cloud microphysics (*AR*); 4) full aerosol effects for both microphysics and radiation (*AMR*); 5) same as *AMR,* but the aerosol coupling used all aerosol species except dust (*AMR-ABD*); 6) same as *AMR,* but using only black and organic carbon and ignoring all other aerosol species (*AMR-CO*); 7) same as *AMR,* but using only sea salt and ignoring all other aerosol species (*AMR-SSO*); and 8) same as *AMR,* but using only dust and ignoring all other aerosol species (*AMR-DO*).

4. Simulation Results

a. Comparison between simulations and observations

Simulated storm tracks and intensities (in terms of minimum sea-level pressure, MSLP) for each experiment are shown in Fig. 7 along with the best track information provided by the National Hurricane Center (NHC). The initial points of all curves represents the model time at 12h (1200UTC 10 September 2012) due to the fact that there was no NHC best track report for the first 12 hours of model integration. Each of the experiments follows a similar track (Fig. 7a), diverging only toward the end of the simulations after 120 h. The initial low pressure centers are displaced to the northeast of the best track position and remain to the north of the best track through the first

36-42 h, after which time the positions shift to the west of the best track position as the storms get more organized. The simulated storms move north-northwestwardly about 100 km to the west of the best track between 48 and 96 hours, but close to each other, and move with a forward motion that is too slow compared to the observed track after 96 hours. Due to a lag in the turn to the east in the simulations (roughly about 12 hours later than the best track), the simulated tracks are greater than 200-300 km to the west of the best track by 120 h. For the remainder of the simulations, the storms make a much slower turn to the east as Nadine came under the influence of enhanced deep layer (200-850 hPa) westerly shear associated with an upper-tropospheric trough.

The simulated storm intensities remain clustered together through about 84 hours (Fig. 7b), followed by gradual divergence of the solutions. The simulations intensify slowly through about 66 h, and then begin a period of more rapid intensification through the end of the period. In contrast, the real storm underwent a period of significant intensification about 24 hours earlier than the simulations and then developed more slowly thereafter. Many of the simulations undergo a brief pause in intensification between 96-120 h, and then resume intensification. The cause of the pause is unknown. The Ctrl and AMR-CO simulations produce the strongest storms while the AMR and AMR-ABD cases produce the weakest storms at 168h, with the AMR case producing a time series most in line with the best track intensity. This result shows that the inclusion of the effect of the real-time predicted aerosol in hurricane simulations can be vitally important for increasing the accuracy of the forecasted track and intensity of numerical models. The discrepancy between the simulated and observed intensities can be explained as follows. In this particular region of the Atlantic (Fig. 8, from domain 3), the ocean is roughly 2-3 K warmer in the western half of the domain than the eastern half, and is coldest in the northeastern quadrant of the domain. Due to the westward shift, later eastward turning, and slower motion of the simulated storms compared to the best track, the simulated storms have much longer residence times over the warmest water, providing greater fuel for intensification compared to the actual storm, and thereby enabling greater total intensification.

Since *AMR* has the most realistic representation of aerosol effects and produced the best simulated intensity overall for Nadine (especially after 96h) in this study, it will be used for comparisons to the observations in the following sections. Figure 9 shows the WRF-simulated AOD from domain 2 from *AMR* and the MODIS AOD. On 11 September, both the simulation and MODIS (Figs. 9a, b) depict a dust outbreak that has recently emerged from Africa with similar shape and AOD, although the simulated AOD is smaller than that seen in MODIS. The leading edge of the dust outbreak has started curving around the western side of Nadine; this AOD could not readily be detected by MODIS due to cloud cover. On 15 September (Figs. 9c, d), the dust outbreak has move farther westward and then northward with the storm. The shape of the SAL outbreak has transformed into a swan-like pattern in which the "neck" at the western end of the dusty air mass is associated with northward transport around the eastern and northern sides of Nadine and roughly parallels the simulated storm track in Fig. 7a. At this stage, the simulated dust has dissipated faster than observed, with lower AODs than seen by MODIS. Despite the faster decrease in dust amount, the simulated AOD pattern generally compares well with the MODIS AOD evolution. It should also be pointed out that there is a high-AOD region in the upper-left corner of the domain that is partially visible near a region of clouds in the MODIS image. This high-AOD region was not associated with the Saharan dust and was transported from forest fires in the northwestern U.S. (see Fig. 6) by the upper-tropospheric westerlies. The potential effect of this black carbon on Nadine will be discussed later in the paper.

The along-the-flight-track simulated cross-sections in Fig. 10 from *AMR* is provided for a direct comparison with the aircraft observations in Fig. 2. The flight crossed over clouds to the west of the storm center between 1800-1930 UTC and over the storm core between 2100-2240 UTC on 11 September (the second and third north-south tracks from the west, respectively, in Fig. 9b). The green arrows in Fig. 10a highlight two regions of SAL dust near the storm core associated with the arc of low AOD on the southwestern side of the storm (Fig. 9a). The dust patch to the north (near 24°N, 2045 UTC) of the storm is consistent with the CPL-observed aerosol backscatter noted in Fig. 2. This dust is coincident with a region of mid-level (750-550 hPa) dry and warm air (Figs. 10b, 10c), likely associated with the SAL, that exists much closer to the storm than suggested by the dust itself. Only the 2045 UTC dropsonde measurements (Fig. 3) indicated the presence of SAL air in this region, with the SAL air confined to ~800-700 hPa. Subsequent dropsondes located closer to the core did not indicate SAL air, suggesting that the SAL intrusion in the model was either too extensive or occurring too early in the model compared to observations. The dust to the south of the storm core region (near 15°N, 2230 UTC) is associated with a very narrow zone of warm and dry air. However, due to the overlying deep convective cloud cover, CPL wasn't able to detect the dust in this region. The simulated temperature perturbation (Fig. 10c) along the flight track between 2130 and 2230 UTC 11 September shows the existence of the tropical storm warm core that could not be detected by S-HIS due to the convective cloud cover.

b. Aerosol evolution and and evidence for SAL intrusion into Nadine

One of the concerns of Braun (2010) about SAL-TC interaction studies was the attribution of storm weakening to the effects of the SAL based on the proximity of the SAL to the storm rather than a direct demonstration of SAL air influencing the storm. In this section, we provide evidence for vertical transport (and by implication IN production) and removal of aerosols within Nadine, and at least one direct mechanism by which the SAL may have influenced Nadine.

The evolution of AOD between 48h and 168h of the simulation (valid at 0000 UTC 12 to 17 September at 24-h intervals) is shown in Fig. 11 along with the sea-level pressure field. As Nadine moved northwestward between 48 and 120 h, the high-AOD SAL airmass gradually encroached around the northeastern quadrant of the storm, although it did not generally get much farther around than the northern portion of the storm. While this AOD was predominately associated with dust, low levels of carbon-based aerosols were present and accounted for about 0.5% of the aerosol mass in this high-AOD airmass (not shown) and were traced back to fires in some part of Africa near the equator. AOD values diminished over the period due to a combination of sedimentation and wet removal, with AOD values by 120 h up to ~0.6. Sauter and L'Ecuyer (2017) suggested that tropical cyclones can remove up to 95% of the nearby aerosols through wet removal. Dust amounts continue to decline near the storm thereafter.

Another region of high AOD was also apparent over the northeastern U.S. at 48 h (Fig. 11a). During the next 72 hours, this aerosol was transported eastward and then southeastward by the upper-level flow. By 144 h (Fig. 11e), this other source of aerosols had reached Nadine's periphery. Using information from the model outer domains (D1 and D2) and MERRA-2, this aerosol was traced back to carbon sources originating from forest fires in the northwestern U.S. that had occurred a few days earlier (not shown here). The impact of these carbon aerosols on Nadine is probably small given the late stage at which they reached Nadine.

To demonstrate the extent to which the different aerosol types were being drawn into Nadine's clouds and precipitation, and hence their ability to impact the cloud microphysics, Fig. 12 shows the cloud (ice, snow and graupel) hydrometeor mixing ratios and aerosol mixing ratios in the 300-100 hPa layer after 96 h of simulation. Saharan dust and sea salt are not likely to be present in the upper troposphere unless transported upward by deep convection. Carbon can potentially be injected into the upper troposphere by deep smoke plumes, and so their presence aloft does not preclude sources other than convection. At 96 h, the precipitation pattern (Fig. 12a) shows a well-defined eyewall (centered near 55°W, 25°N) and extensive outer rainbands to the north and southeast of the inner-core region. These rainbands extend into the region of AOD>0.2 and therefore represent areas of deep convection capable of significant upward transport of aerosols. The dust distribution in the 300-100 hPa layer (Fig. 12b) shows maximum values to the northeast of Nadine's center in the region of the outer rainband, indicating that the rainband is a significant source of the upper-tropospheric dust. The high values of dust extending to the east and southeast of Nadine are found within the outflow layer and suggest significant horizontal transport away from the rainbands. Near the inner core of Nadine, there is very little dust aloft, suggesting that dust is not not being transported upward in the eyewall and, therefore, not likely getting into the eyewall at lower levels. The peak upper-tropospheric dust amounts are about 10-20% of the peak amounts in the lower troposphere. Sauter and L'Ecuyer estimated from CALIPSO and CloudSat data that lofted dust represented about 1-2% of lower-tropospheric dust amounts after the passage of tropical cyclones, which suggests that the NUWRF model is potentially underestimating wet removal of aerosols.

The spatial pattern of carbon (Fig. 12d) at upper levels is quite similar to dust, although the magnitudes are about two orders of magnitude smaller, suggesting a similar mechanism for carbon vertical transport. Sea salt (Fig. 12c), with magnitudes about an order of magnitude smaller than dust, has relatively higher values within the outflow layer originating near the northern rainband, and also shows a clear pattern of upward transport in the eyewall. This pattern is largely expected since sea salt is present over an extensive area of the ocean and is maximum in the high-wind region of the inner-core region (not shown).

The key takeaway here is that dust and carbon are clearly getting into the outer bands of Nadine, but not into the inner core of the storm. Studies by Khain et al. (2008), Zhang et al. (2009), Cotton et al. (2012), and Herbener et al. (2014) suggest that if the aerosols invigorate convection (Khain et al. 2005; van den Heever et al. 2006; Jenkins et al. 2008; Storer et al. 2014), then their presence in the outer rainbands would be expected to strengthen the rainband convection at the expense of convection in the eyewall (possibly through decreased inflow to the inner core, compensating subsidence over the eyewall, and increased outer-band cold pools), thereby weakening the storm. Rosenfeld et al. (2007) also suggested that seeding of clouds on the tropical cyclone periphery could weaken storms. Hence, the weakening of the simulated Nadine (as in case AMR) is consistent with the diagnosis of aerosols being ingested into the outer bands of Nadine, but not into the eyewall.

Besides the aerosol impacts of the SAL, the SAL can influence storm development as a result of its associated thermodynamic and wind characteristics, i.e., near neutral static stability above the base of the SAL, dry air, and enhanced easterly flow (primarily along the southern edge of the SAL). Figure 13 shows west-to-east cross sections through the center of the storm of temperature perturbation (shading), defined as the perturbation from the domain-averaged temperature at 0 h, and dust mass (contours) from *AMR* every 24 h starting at 48 h. Figure 13 shows the corresponding relative humidity fields. At 48h, the warm core (Fig. 13a) has formed between 44° and 50°W as the storm starts to intensify. The SAL is seen just to the east of Nadine (east of about 41°W), with the dust layer extending to just above 500 hPa and the temperature perturbation field being characterized by warm air between 950 and 700 hPa and colder air between 700 and 500 hPa. This dipole structure is associated with the nearly dry adiabatic lapse rate as described by Carlson and Prospero (1972), Karyampudi and Carlson (1988), and Braun (2010). The relative humidity pattern shows a broad area of moist conditions associated with the storm. In the SAL, dry air is seen between ~900-700 hPa, while higher relative humidity of ~50-60% is near the top of the SAL. Very dry non-Saharan air is present above the SAL and extends downward into the uppermost part of the dust layer. A tongue of this drier air appears to extend downward along the leading edge of the dust layer. During the next 48 hours, the storm continues its intensification as indicated by a strengthening warm core (Fig. 13b and 13c), while the SAL moves closer to the storm core. This inward penetration of the SAL is particularly apparent in the coresponding relative humidity field (Figs. 14b and 14c) as the region of higher humidity significantly narrows from about 10° wide at 48 h to ~6° wide by 96 h. Dust near the leading edge of the SAL is transported upward into the upper troposphere by the outer rainbands and then transported outward by the outflow of the storm (indicated by the lowest contour level), as discussed above. By 96 h (Fig. 13c), the leading edge of the dust layer and the depth of the SAL warm layer becomes shallower, and this change becomes even more pronounced for the entire SAL air mass by 120 h (Figs. 13d and 14d). The progression to a shallower and colder SAL airmass may be the result of the effects of aerosol particle sedimentation, wet removal, and net radiative cooling of the layer. Also notable about the period from 96-120 h is that the leading edge of the SAL resides underneath part of the warm core, the warm air SAL reaches the surface, and the colder air in the upper SAL layer is extending downward toward the surface close to the storm.

The intrusion of the SAL air into the outer rainbands of Nadine is a source of enhanced convective downdrafts. Figure 15 shows 950-hPa equivalent potential temperature, θ_e, at 120 h. At this time, the leading edge of the lower θ_e air associated with the SAL at the latitude of the storm center is near 54°W. A broad area of low θ_e air is located northeast of the storm center and a narrow band of cold pools extends southward just east of 54°W along the outer band that separates SAL air from non-SAL air (Fig. 5). The presence of the low θ_e air, along with the cross sections in Figs. 13 and 14, strongly suggest that the SAL is contributing to enhanced cold pool activity in Nadine. Unfortunately, it is not possible to quantify the impact of the enhanced cold pool activity on storm intensity.

c. Aerosol impacts on simulated tracks and minimum sea-level pressures

In general, the various model experiments show that aerosols have little impact on storm intensity through 84 hours and track through 120 hours. The minimal response of storm track is consistent with Cotton et al. (2012). The simulated intensities begin to diverge around 96 h, with *Ctrl*, *AMR,* and *AMR-ABD* (dark blue, red, and orange lines, respectively, in Fig. 7b) producing the weakest storms. However, the differences between simulations are not necessarily maintained throughout the simulations. For example, *AMR-SSO* is stronger than *Ctrl* prior to 120 h, but then becomes weaker than *Ctrl*. Similarly, *AMR-DO* is stronger than *Ctrl* up to 114 h, but then becomes weaker. In general, all simulations are stronger than observed.

Examining simulated intensities at 120 h (prior to the significant track divergence), simulations *AMR* and *AMR-ABD* result in the weakest storms while *AMR-DO* is between *AMR* and *Ctrl* (just 6 hours earlier, *AMR-DO* was almost identical to *Ctrl*). Cases *AMR-CO* and *AMR-SSO* are similar to *Ctrl* at 120 h. Subsequent intensity differences are difficult to interpret because of the significant differences in storm track. The results show that dust is not the only aerosol species potentially affecting the intensification of Nadine. Although the differences between the simulations vary with time, when one compares these individual aerosol-species cases (*AMR-SSO*, *AMR-CO*, and *AMR-DO*) to the combined-aerosol cases (*AMR-ABD* and *AMR*), the results suggest that overall aerosol loading may be more important than the specific aerosol species, with greater aerosol amount leading (correctly) to greater reduction of storm intensity. However, one must be careful in this interpretation. The small values of carbon near Nadine (Fig. 12) are consistent with the intensity of *AMR-CO* being close to that of *Ctrl*. Total loading of sea salt is lower than dust, but more areally extensive, which may have allowed AMR-SSO to produce a weaker intensity after 120 than the case with only dust (AMR-DO).

Similarly, it is insufficient to consider aerosol impacts with either radiative or microphysical impacts alone (AR and AM). By 120 h, both cases produce similar storm intensities compared to Ctrl (again, significant variations with time), with radiative effects producing a stronger impact than microphysical effects in the longer term. Both cases are more intense than the case when both aerosol interactions are active (AMR), suggesting that both influences may act in concert to weaken storms, although this result may be storm dependent.

d. Aerosol effects on hydrometeor profiles

Eight simulations were conducted to evaluate the impact of different aerosols on Nadine, and this section will focus on the aerosol impacts on cloud and precipitation hydrometeor profiles. Figures 16a and 16b show area-averaged cloud and precipitation hydrometeor profiles, respectively, from *Ctrl*. The area over which the profiles are averaged corresponds to a 900×900km^2 box following the storm center. The melting level occurs around 550-600 hPa. Cloud ice tends to peak near 200 hPa and extends from about 300-100 hPa (Fig. 16a). Cloud liquid water peaks around 800 hPa and extends from just above the surface to about 500 hPa. Snow and graupel (referred to hereafter as precipitation ice, shown togethers by shading in Fig. 16b) show a relatively sharp peak near 400-500 hPa, while the rain profile has a broader peak at earlier times and then develops a narrower peak near 800-900 hPa at later times. A clear diurnal cycle is also evident in the precipitation mixing ratios (Fig. 16b), with maximum values around 15-18 UTC.

The remaining panels in Figs. 16 show the differences in hydrometeors between the sensitivity simulations and *Ctrl*. For the *AMR* simulation, differences in cloud ice vary across both positive and negative values, while cloud water shows a consistent reduction that grows with time (Fig. 16c). In both rain and precipitation ice (Fig. 16d), there are diurnally varying periods of decreased mixing ratios. When only the microphysical impacts of the aerosols are included in the simulation (*AM*, Figs. 16e, 16f), a very similar pattern of reduced hydrometeors is seen, although with smaller magnitudes. In contrast, when only the radiative impacts of aerosols are included (*AR*, Figs. 16g, 16h), cloud liquid water and rain show small deceases before 15 September, followed by periods of increased mixing ratios. Changes in precipitation ice are smaller than in *AMR*, with increased mixing ratios from mid 14 September through mid 15 September. Even though aerosol radiative effects increase hydrometeor production in *AR* at later times, they not only don't provide a similar increase in *AMR*, they actually increased the negative impacts on hydrometeor production. This result underscores the fact that a strong non-linear interaction exists among aerosols, radiation, and cloud microphysics.

The sensitivity of the microphysics to individual aerosol species is shown in Fig. 17, which also shows differences from the mean hydrometeor profiles of *Ctrl* in Figs. 16a and 16b. Both cases with sea salt only (Figs. 17a, 17b) and carbon only (Figs. 17c, 17d) produce reductions in the hydrometeor mixing ratios (except cloud ice). Profiles for *AMR_ABD* (Figs. 17e, 17f), which includes sea salt and carbon together, show quantitatively similar decreases as in *AMR_SSO* and *AMR_CO* individually and, like *AM* and *AR*, are not a linear combination of the two cases. These results are significant as sea salt exists everywhere in the lower troposphere over the ocean and is in especially high concentrations under high windspeed conditions such as in tropical cyclones (not shown). It is difficult to determine whether the carbon aerosol that produced the reduced hydrometeors during the mature stage originated from the forest fires in the northwestern U.S. (Fig. 11) or from the carbon coincident with the Saharan dust (Fig. 12d). The results suggest that, while emphasis is often placed on the effects of dust, in some events it could be difficult to produce accurate hurricane intensity and, to a lesser extent, track forecasts without considering the microphysical and radiative effects of all aerosol species.

The simulation with dust only (*AMR_DO*, Figs. 17g, 17h) is different. While it produces reduced cloud water, it also leads to periods of enhanced cloud ice, precipitation ice, and rain. These microphysical impacts might account for the dust-only case producing a stronger storm than the all-but-dust case (A*MR_ABD*) despite the fact that dust is the dominant aerosol type. Although one cannot directly relate changes in hydrometeors to changes in storm intensity relative to *Ctrl* (e.g., *AMR_CO* produces reductions in hydrometeors yet has an intensity comparable to *Ctrl*), it is possible that enhancements in hydrometeor production offset other negative impacts of dust in *AMR_DO*.

5. Summary and Discussion

In this study, we utilized the NU-WRF model with aerosol-cloud-radiation coupling and an inline aerosol distribution forecast component to conduct a sensitivity study of the impact of dust from the SAL and other aerosols on Hurricane Nadine (2012). Observations from the HS3 field experiment were analyzed and compared to the simulation. During the early stage of the storm, data from HS3's first flight over Nadine showed an environment on the western side of the storm that was largely devoid of significant SAL air, with only a small and shallow (up to 800 hPa) aerosol layer seen by lidar observations. In contrast, in the eastern portion of the storm, an extensive 5-km deep dust layer was observed, with warm and dry air between 900 to 650 hPa. MODIS data suggested a SAL air mass that was rapidly encroaching on the eastern side of Nadine, but that was only just beginning to wrap around the northern side during this first flight. Dropsonde data collected in the second HS3 flight three days later (Fig. 5) during the mature stage showed that the lower troposphere in the region to the east and north of Nadine's outer rainband was dry and warm relative to other sectors of the storm and was associated with the SAL. In the upper troposphere, very dry air was impinging on the western side of Nadine as strong vertical wind shear was inhibiting intensification above minimal hurricane status (B16). Thermodynamic conditions changed markedly across the outer rainband to the southeast of the storm center, indicated by two dropsonde profiles in Fig. 5d, suggesting the rainband formed a boundary between SAL air to the east and non-SAL air to the west.

The model simulation with interactive dust did a reasonable job of capturing these key features of the storm. There were, however, some notable departures of the simulations from the observations particularly in terms of storm track and intensity. The simulated storm tracks consistently had a westward bias and slower northward motion so that the storm moved over a region of higher sea surface temperatures for a longer period of time, and then made the sharp turn to the east significantly later than the observed storm, possibly as a result of weaker westerly vertical wind shear in the simulations. The passage over warmer SSTs, the slower motion, and reduced shear impacted the simulated storm intensities, causing more sustained intensification well after the observed storm had stopped intensifying. However, the simulations still provide useful diagnostics for examining the potential influences of dust and the SAL on the evolution of Nadine.

In several simulations, aerosols led to storm strengthening, followed by weakening relative to the *Ctrl* simulation. There is clear evidence of aerosols getting into the outer bands, in the form of vertical transport of aerosols to the upper troposphere and within the storm outflow; however, we saw little evidence of aerosol vertical transport in the inner core other than for sea salt, which is maximized in the inner-core boundary layer. The simulations imply that the early intensification may have resulted from aerosols, particularly sea salt, in the inner-core region. Indeed, the simulation with sea salt only (*AMR_SSO*) produced the strongest initial intensification (out to 106 h) before a period of brief weakening and subsequent slow intensification. The intensity trends may have resulted from aerosols invigorating convection in the inner core at early times, followed by invigoration of outer rainbands at later times, as in Cotton et al. (2012).

In most aerosol experiments (all aerosols, sea salt only, carbon only, and all but dust), aerosols led to a reduction in cloud liquid water, rain, snow, and graupel. Reductions in the sea-salt-only and carbon-only cases were similar and comparable to the reduction of hydrometeors in the all-but-dust (i.e., salt and carbon) case, showing that the combined case was not the sum of the individual cases. The dust-only case, while also leading to reduced cloud water, produced periods of enhanced growth of rain, snow, and graupel. The mechanism for this enhancement is not known. In the simulations, CCN activation is low due to the coarse grid resolution, so the aerosols primarily play a role as IN and in the radiative effects of aerosols, and these effects over the course of the simulations do not lead to clear explanations about interactions with hurricane internal processes to affect hydrometeors or storm intensity.

Dunion and Velden (2004) found that dry SAL air can contribute to convective downdrafts and that elevated warm air can suppress convection. In this study, a variation of these effects is identified. We first note that, as seen in previous studies, the SAL is not warm throughout its depth, but is colder than its environment in the upper part of the layer. In the aerosol-interactive simulation (*AMR*), a region of strong easterlies associated with the AEJ was impinging on the eastern side of Nadine, and at the leading edge of these easterlies, cool and dry air near the top of the SAL was being ingested into the outer-band convection in Nadine. This midlevel low equivalent potential temperature air gradually lowered toward the surface and eventually contributed to significant cold pool activity in the eastern rain band and in the northeast quadrant of the storm (Fig. 15). One would anticipate that such enhanced downdraft activity could lead to weakening of the storm, but it is not presently possible to quantify this impact without somehow excising the SAL from the simulation. Well-designed idealized or ensemble simulations might allow for quantification of this process.

Acknowledgements

This research effort is supported by the NASA headquarters Weather and Atmospheric Dynamics (NNH16ZDA001N-WEATHER) and Modeling, Analysis, and Prediction (NNH16ZDA001N-MAP) Programs. The authors are grateful to Drs. Gail Skofronick-Jackson, Ramesh Kakar, and David Considine at NASA headquarters for their support of this research.

Data Availability Statement

All data collected during the HS3 field campaign for Nadine (2012), including those analyzed for this study, are available at https://ghrc.nsstc.nasa.gov/home/projects/hs3. In addition, all model simulations were conducted at the NASA Center for Climate Simulation (NCCS). All model data generated for this study are currently archived on the NCCS mass storage systems. Due to the extremely large amount of data, it would be impractical to upload data to a public domain repository. However, the authors will be happy to provide the model data upon request.

References

Andreae, M. O., and D. Rosenfeld, 2008: Aerosol–cloud–precipitation interactions. Part 1. The nature and sources of cloud-active aerosols. *Earth-Science Reviews*, 89, 13-41. https://doi.org/10.1016/j.earscirev.2008.03.001.

Braun, S. A., 2010: Re-evaluating the role of the Saharan Air Layer in Atlantic tropical cyclogenesis and evolution. *Mon. Wea. Rev.*, 138, 2007–2037.

——, J. A. Sippel, C.-L. Shie, and R. A. Boller, 2013: The Evolution and Role of the Saharan Air Layer during Hurricane Helene (2006) . *Mon. Wea. Rev.,* **141,** 4269-4295.

——, P. A. Newman, and G. M. Heymsfield, 2016: NASA's Hurricane And Severe Storm Sentinel (HS3) Investigation. *Bull. Amer. Meteor. Soc.*, **97**, 2085–2102, doi:10.1175/BAMS-D-15-00186.1.

Brown, D. P., 2013: Tropical Cyclone Report Hurricane Nadine (2012). *Report AL142012*, National Hurrucane Center, Miami, Florida.

Carlson, T. N., and S. G. Benjamin, 1980: Radiative heating rates for Saharan dust. *J. Atmos. Sci.*, **37**, 193-.213.

Carlson, T. N., and J. M. Prospero, 1972: The large-scale movement of Saharan air outbreaks over the northern equatorial Atlantic. J. Appl. Meteor., 11, 283–297.

Chen, F. and J. Dudhia, 2001: Coupling an advanced land surface - Hydrology model with the Penn State - NCAR MM5 modeling system. Part I: Model implementation and sensitivity. *Mon. Weather Rev.*, **129**, 569-585.

Chen, S.-H., S.-H. Wang, and M. Waylonis, 2010: Modification of Saharan air layer and environmental shear over the eastern Atlantic Ocean by dust-radiation effects. J. Geophys. Res., Vol. 115, D21202, doi:10.1029/2010JD014158.

Chin, M., R. B. Rood, S.-J. Lin, J.-F. Müller, A. M. Thompson, 2000a. Atmospheric sulfur cycle simulated in the global model GOCART: model description and global properties. J. Geophys. Res. 105 (D20), 24671e24687. http://dx.doi.org/ 10.1029/2000JD900384.

——, D. L. Savoie, B. J. Huebert, A. R. Bandy, D.C. Thornton, T. S. Bates, P. K. Quinn, E. S. Saltzman, and W. J. De Bruyn, 2000b. Atmospheric sulfur cycle simulated in the global model GOCART: comparison with field observations and regional budgets. J. Geophys. Res. 105 (D20), 24689e24712. http://dx.doi.org/ 10.1029/2000JD900385.

——, T. Diehl, O. Dubovik, T. F. Eck, B. N. Holben, A. Sinyuk, and D. G. Streets, 2009: Light absorption by pollution, dust, and biomass burning aerosols: A global model study and evaluation with AERONET measurements, *Annales Geophysicae,* **27**, 3439-3464.

Chou M.-D., and M. J. Suarez, 1999: A solar radiation parameterization for atmospheric studies. NASA Tech. Rep. NASA/TM-1999-10460, vol. 15, 38 pp

Chou M.-D., and M. J. Suarez, 2001: A thermal infrared radiation parameterization for atmospheric studies. NASA/TM-2001-104606, vol. 19, 55pp

Cotton, W. R., H. Zhang, G. M. McFarquhar, and S. M. Saleeby, 2007: Should we consider polluting hurricanes to reduce their intensity? J. Weather Mod., 39, 70-73.

——, G.M. Krall, and G.G. Carrió, 2012: Potential indirect effects of aerosol on tropical cyclone intensity: convective fluxes and cold-pool activity. *Tropical Cyclone Research and Review*, 1(3): 293-306.

Dee, D. P., and co-authors, 2011: The ERA-Interim reanalysis: configuration and performance of the data assimilation system. *Q. J. R. Meteorol. Soc.*, **137**, 553–597.

Demott, P. J., A. J. Prenni, X. Liu, S. M. Kreidenweis, M. D. Petters, C. H. Twohy, M. S. Richardson, T. Eidhammer , and D. C. Rogers, 2010: Predicting global atmospheric ice nuclei distributions and their impacts on climate. Proceedings of the National Academy of Sciences, 107 (25), 11217–11222.

Dunion, J. P., and C. S. Velden, 2004: The impact of the Saharan air layer on Atlantic tropical cyclone activity. *Bull. Amer. Meteor. Soc.*, 84, 353–365.

Grell, G. A. and D. Dévényi, 2002: A generalized approach to parameterizing convection combining ensemble and data assimilation techniques. *Geophys. Res. Lett.*, **29**, 1693, doi: 10.1029/2002GL015311.

Herbener, S. R., S. C. van den Heever, G. G. Garrio, S. M. Saleeby, and W. R. Cotton 2014: Aerosol Indirect Effects on Idealized Tropical Cyclone Dynamics. *J. Atmos. Sci.,* **71,** 2040-2055.

Hong, S.-Y., and J.-O. J. Lim, 2006: The WRF Single-Moment 6-Class Microphysics Scheme (WSM6), J. Korean Meteor. Soc., 42, 129–151.

——, 2007: Stable Boundary Layer Mixing in a Vertical Diffusion Scheme. The Korea Meteor. Soc., Fall conference, Seoul, Korea, Oct. 25-26.

Jenkins, G. S., A. Pratt, and A. Heymsfield, 2008: Possible linkages between Saharan dust and tropical cyclone rain band invigoration in the eastern Atlantic during NAMMA-06. Geophys. Res. Lett., **35**, L08815, doi:10.1029/2008GL034072.

Jones, C., N. Mahowald, and C. Luo, 2004: Observational evidence of African desert dust intensification of easterly waves. *Geophys. Res. Lett.*, 31, L17208, doi:10.1029/2004GL020107.

Karyampudi, V. M., and T. N. Carlson, 1988: Analysis and numerical simulations of the Saharan air layer and its effect on easterly wave disturbances. J. Atmos. Sci., 45, 3102–3136.

——, and Coauthors, 1999: Validation of the Saharan dust plume conceptual model using lidar, Meteosat, and ECMWF data. Bull. Amer. Meteor. Soc., 80, 1045–1075.

——, and H. F. Pierce, 2002: Synoptic-scale influence of the Saharan air layer on tropical cyclogenesis over the eastern Atlantic. Mon. Wea. Rev., 130, 3100–3128.

Khain, A., D. Rosenfeld, and A. Pokrovsky, 2005: Aerosol impact on the dynamic and microphysics of deep convective clouds. *Q. J. R. Meteorolf. Soc.*, **131**, 2639-2663.

——, N. Cohen, B. Lynn, and A. Pokrovsky, 2008: Possible aerosol effects on lightning activity and structure of hurricanes. *J. Atmos. Sci.*, **65**, 3652-3677.

——, B. Lynn, and J. Dudhia, 2010: Aerosol effects on intensity of landfalling hurricanes as seen from simulations with WRF model with spectral bin microphysics. *J. Atmos. Sci.*, **67**, 365–384.

Koehler, K. A., and Co-authors, 2006: Water activity and activation diameters from hygroscopicity data – Part II: Application to organic species. *Atmos. Chem. Phys.*, 6, 795–809 .

Lang, S., W.-K. Tao, R. Cifelli, W. Olson, J. Halverson, S. Rutledge, and J. Simpson, 2007: Improving simulations of convective systems from TRMM LBA: Easterly and westerly Regimes. *J. Atmos. Sci.*, **64**, 1141-1164.

——, W.-K. Tao, X. Zeng, and Y. Li, 2011: Reducing the Biases in Simulated Radar Reflectivities from a Bulk Microphysics Scheme: Tropical Convective Systems. *J. Atmos. Sci.*, **68**, 2306-2320.

Lau, K. M., and J. M. Kim, 2007a: How nature foiled the 2006 hurricane forecasts. Eos, Trans. Amer. Geophys. Union, 88 (9), 105–107.

——, and ——, 2007b: Cooling of the Atlantic by Saharan dust. Geophys. Res. Lett., 34, L23811, doi:10.1029/2007GL031538.

Liu, Y., and P. H. Daun, 2004: Parameterization of the Autoconversion Process. Part I: Analytical Formulation of the Kessler-Type Parameterizations. *J. Atmos. Sci.,* **61**, 1539-1548.

Matsui, T., and coauthors, 2013. GPM satellite simulator over ground validation sites. Bull. Am. Meteor. Soc. 94, 1653e1660. http://dx.doi.org/10.1175/BAMS-D- 12-00160.1

——, J. Santanell, J. J. Shi, W.-K. Tao, D. Wu, C. Peters-Lidard, E. Kemp, M. Chin, D. Starr, M. Sekiguchi, F. Aires, 2014. Introducing multi-sensor satellite radiance-based evaluation for regional earth system modeling. J. Geophys. Res. Atmos. 119, 8450e8475. http://dx.doi.org/10.1002/ 2013JD021424

——, S. Q. Zhang, W.-K. Tao, S. Lang, C. Ichoku, and C. Peters-Lidard, 2018: Impact of Radiation Frequency, Precipitation Radiative Forcing, and Radiation Column Aggregation on Convection-Permitting West African Monsoon Simulations, *Climate Dynamics*, 1-21, https://doi.org/10.1007/s00382-018-4187-2

Messager, C., D. J. Parker, O. Reitebuch, A. Agusti- Panareda, C. M. Taylor, and J. Cuesta, 2010: Structure and dynamics of the Saharan atmospheric bound- ary layer during the West African monsoon onset: Observations and analyses from the research flights of 14 and 17 July 2006. *Quart. J. Roy. Meteor. Soc.*, **136**, 107–124, doi:10.1002/qj.469.

Meyers, M. P., P. J. DeMott, and W. R. Cotton, 1992: New Primary Ice-Nucleation Parameterization in an Explicit Cloud Model. J. Appl. Meteor., **31**, 708-721.

Monin, A. S. and A. M. Obukhov, 1954: Basic laws of turbulent mixing in the surface layer of the atmosphere. *Contrib. Geophys. Inst. Acad. Sci. USSR*, **24**, 163-187. (in Russian)

Peters-Lidard, C.D., and coauthors, 2015: Integrated modeling of aerosol, cloud, precipitation and land processes at satellite-resolved scales. *Environmental Modelling & Software*, **67**, 149–159, doi:10.1016/j.envsoft.2015.01.007.

Prospero, J. M., and T. N. Carlson,1981: Saharan air outbreaks over the tropical North Atlantic. Pure Appl. Geophys., 119, 677–691.

Reale, O., W. K. Lau, K.-M. Kim, and E. Brin, 2009: Atlantic tropical cyclogenetic processes during SOP-3 NAMMA in the GEOS-5 Global Data Assimilation and Forecast System. *J. Atmos. Sci.*, **66**, 3563-3578.

Rosenfeld, D., A. Khain, B. Lynn, and W. L. Woodley, 2007: Simulation of hurricane response to suppression of warm rain by sub-micron aerosols. *Atmos. Chem. Phys.*, **7**, 3411–3424.

——, U. Lohmann, G. B. Raga, C. D. O'Dowd, M. Kulmala, S. Fuzzi, A. Reissell, and M. O. Andreae, 2008: Flood of drought: How do aerosols affect precipitation? *Science*, **321**, 1309-1313.

——, M. Clavner, and R. Nirel, 2011: Pollution and dust aerosols modulating tropical cyclone intensities. *J. Atmos. Res.*, **102**, 66–76, doi:10.1016/j.atmosres.2011.06.006.

——, W. L. Woodley, A. Khain, W. R. Cotton, G. G. Carrio , I. Ginnis, and J. H. Golden, 2012: Aerosol effects on micro- structure and intensity of tropical cyclones. *Bull. Amer. Meteor. Soc.*, **93**, 987–1001, doi:10.1175/BAMS-D-11-00147.1.

Sauter, K., and T. S. L'Ecuyer, 2017: Observational evidence for the vertical redistribution and scavenging of Saharan dust by tropical cyclones, *Geophys. Res. Lett.*, **44**, 6421–6430, doi:10.1002/2017GL074166.

Shi, J. J., W.-K. Tao, T. Matsui, A. Hou, S. Lang, C. Peters-Lidard, G. Jackson, R. Cifelli, S. Rutledge, and W. Petersen, 2010: Microphysical Properties of the January 20-22 2007 Snow Events over Canada: Comparison with in-situ and Satellite Observations. *Journal of Applied Meteorology and Climatology*. 49(11), 2246–2266.

——, T. Matsui, W.-K. Tao, Q. Tan, C. Peters-Lidard, M. Chin, K. Pickering, N. Guy, S. Lang, and E. Kemp., 2014: Implementation of an Aerosol-Cloud Microphysics-Radiation Coupling into the NASA Unified WRF: Simulation Results for the 6-7 August 2006 AMMA Special Observing Period. *Quart. J. Roy. Meteor. Soc.*, **140**, 2158-2175, doi:10.1002/qj.2286.

Skamarock, W. C., and Coauthors, 2008: A description of the advanced research WRF version 3. NCAR Tech. Note NCAR/ TN-4751STR, 88 pp.

Storer, R. L., S. C. van den Heever, and T. S. L'Ecuyer, 2014: Observations of aerosol-induced convective invigo- ration in the tropical east Atlantic. *J. Geophys. Res. Atmos.*, **119**, 3963–3975. doi:10.1002/2013JD020272.

Sun, D., K. M. Lau, and M. Kafatos, 2008: Contrasting the 2007 and 2005 hurricane seasons: Evidence of possible impacts of Saharan dry air and dust on tropical cyclone activity in the Atlantic basin. Geophys. Res. Lett., 35, L15405, doi:10.1029/ 2008GL034529.

Tao, W.-K., and coauthors, 2003: Microphysics, radiation and surface processes in the Goddard Cumulus Ensemble (GCE) model, A Special Issue on Non-hydrostatic Mesoscale Modeling, *Meteorology and Atmospheric Physics,* **82**, 97-137.

——, J.-P. Chen, Z. Li, C. Wang, and C. Zhang, 2012: Impact of aerosols on convective clouds and precipitation. *Rev. of Geophysics*, **50**, RG2001, 62pp., 2012 doi:10.1029/2011RG000369.

Tao, Z., S. A. Braun, J. J. Shi, M. Chin, D. Kim, T. Matsui, and C. Peters-Lidard, 2018: Microphysics and radiation effect of dust on Saharan Air Layer – A HS3 case study. Mon. Wea. Rev, **146**, 1813-1835, doi:10.1175/MWR-D-17-0279.1.

van den Heever, S. C., G. G. Carrió, W. R. Cotton, P. J. DeMott, and A. J. Prenni, 2006: Impacts of nucleating aerosol on Florida storms. Part I: Mesoscale simulations. *J. Atmos. Sci.*, **63**, 1752-1775.

Wu, L., 2007: Impact of Saharan air layer on hurricane peak intensity. Geophys. Res. Lett., **34**, L09802, doi:10.1029/2007GL029564.

Zhang, H., G. M. McFaquhar, S. M. Saleeby, and W. R. Cotton, 2007: Impacts of Saharan dust as CCN on the evolution of an idealized tropical cyclone. *Geophys. Res. Lett.*, **34**, L14812, doi:10.1029/2007GL029876.

——, ——, W. R. Cotton, and Y. Deng, 2009: Direct and indirect impacts of Saharan dust acting as cloud condensation nuclei on tropical cyclone eyewall development. *Geophys. Res. Lett.*, **36**, L06802, doi:10.1029/ 2009GL037276.

List of Table and Figures

Table 1 List of all model experiments.

Figure 1. Best track of Hurricane Nadine (2012) adopted from the National Hurricane Center (NHC), https://www.nhc.noaa.gov/data/tcr/AL142012_Nadine.pdf.

Figure 2. (a) CPL aerosol backscatter ($\times 10^{-2}$ km^{-1} sr^{-1}) along the western portion of the Global Hawk flight path (red line in Fig. 9b) during the 11-12 September 2012 flight. S-HIS (b) relative humidity with respect to water and (c) temperature perturbation for the same flight segment. In (a), regions of weak backscatter beneath high clouds represents noise in the signal rather than particulate backscatter. Temperature perturbations are derived by removing the average temperature from 2000 UTC 11 September to 0600 UTC 12 September, similar to the approach used in Braun et al. (2016). Arrows indicate the times of dropsondes shown in Fig. 3, red for the 1746 UTC and black for the 2045 UTC 11 September dropsondes. In some locations, there is a reversal in the temperature anomalies below 400 hPa and much higher low-level relative humidity, suggesting possible retrieval biases caused by upper-level clouds. Three sets of twin vertical lines indicate the times of aircraft turns to and from the north-south oriented flight legs.

Figure 3. Skew-T log-p diagram showing the 1746 UTC (red) and 2045 UTC (black) dropsonde-derived temperature and dewpoint temperature profiles on 11 September. The 1746 UTC profile was released from the Global Hawk at 51.60°W, 15.43°, while the 2045 UTC dropsonde was released at 46.49°W, 24.24°N.

Figure 4. (a) MODIS aerosol optical depth and clouds for September 13, 2012. The location of a CALIPSO overpass is shown by the black line. Plot generated from NASA Worldview

(https://worldview.earthdata.nasa.gov). The black line also represents the location of the cross-sections shown in (b) CALIPSO 532-nm total attenuated backscatter and (c) aerosol subtype (bottom) at ~1628 UTC 13 September 2012. The figure was adapted from online CALIPSO browse images, version 4.10, at https://www.calipso.larc.nasa.gov/products/lidar/browse_images/production/.

Figure 5. (a) Relative humidity (colored circles) and (b) temperature (colored circles), along with wind barbs (full barb, 5 m s^{-1}; half-barb, 2.5 m s^{-1}; flags, 25 m s^{-1}) at 875 hPa superimposed on the GOES infrared imagery at 0015 UTC 15 September 2012. (c) Same as (a), but for relative humidity at 400 hPa. Dropsonde locations account for dropsonde drift (i.e., uses the GPS-determined position at each height rather than the initial drop location or splashdown location) and storm motion, with positions adjusted to a reference time of 0000 UTC 15 September. (d) Dropsonde temperature and dewpoint temperature profiles at 0105 UTC 15 September (black) in the SAL air mass and 0131 UTC (red) in the non-SAL air mass to the east and west, respectively, of Nadine's outer rainband (see inset in panel b).

Figure 6. NU-WRF double-nested domains used for this study with horizontal grid spacings of 27, 9, and 3 km. The shading represents the analyzed AOD at the model initial time of 0000 UTC September 10, 2012.

Figure 7. (a) Tracks and (b) minimum sea level pressures (MSLP) from the NHC best track and all NU-WRF experiment runs. Marks on all curves indicate a 6-h interval. The first mark in all curves represents the model time at 12h (1200 UTC 10 September 2012). The solid square mark on each curve represents the model time at every 24h.

Figure 8. The ERA-Interim sea-surface temperature analysis every 48 h relative to the initial time of the simulations (00 UTC 10 September). For reference, the plotted storm tracks are from

the NHC best track (black line) and from the simulated tracks for Exps. Ctrl (blue line) and AMR (red line).

Figure 9. NU-WRF/AMR AOD from domain 2 at (a) 1200 UTC 11 and (c) 1200 UTC 15 September compared with daytime MODIS AOD on (b) 11 and (d) 15 September. Superimposed on the satellite image in (b) is the Global Hawk flight track for the 11-12 September flight, with red lines indicating the portion of the flight-track data shown in Fig. 2. Dashed lines indicate the data shown in Fig. 9 of B16. The Global Hawk flight track for the 14-15 September flight is shown in (d), with the flight pattern completed before the time of the image.

Figure 10. Similar to Fig. 2 except derived from Exp. AMR. However, (a) shows the total hydrometeor mixing ratio (g kg^{-1}, shading) from all cloud species while Fig. 2a is the CPL backscatter. Also in (a), dashed contours show dust mixing ratios at 10, 30 and 50 mg kg^{-1}. The row of numbers above each figure indicates the approximate UTC time on September 11 while the numbers just below the top axis in (a) indicates the model hour used to create the cross section. The numbers along the x-axis indcate the latitude (longitude) for the north-south (west-east) tracks. Green arrows in (a) indicate features discussed in the text.

Figure 11. NU-WRF/ARM simulated AOD (shaded), mean sea-level pressure (hPa, contours) and 800-hPa wind (m s^{-1}, vectors) from domain 2 at a) 48h, b) 72h, c) 96h, d) 120h, e) 144h, and f) 168h valid at 0000 UTC of September 12, 13, 14, 15, 16, and 17.

Figure 12. NU-WRF/AMR simulated horizontal distributions (shading) of 300-100 hPa layer-averaged (a) cloud (ice+snow+graupel) mixing ratio (0.01 g kg-1), (b) dust mixing ratio (μg kg-1), (c) sea salt mixing ratio (μg kg-1), and (d) black and organic carbon mixing ratio (μg kg-1) at 96h (valid at 0000UTC 14 September). The black contour shows the AOD=0.2

threshold. Vectors in (a) show 900-hPa winds, while in (b)-(d), vectors indicate 200-hPa winds, taken to be representative of the outflow layer.

Figure 13. West to east cross sections through the storm core of the NU-WRF/AMR temperature perturbation (from the domain mean at 0 h, shaded) and dust (μg/kg-dry air, contours) at a) 48 h, b) 72 h, c) 96 h, and d) 120 h valid at 0000 UTC of September 12, 13, 14, and 15.

Figure 14. Same as Fig. 13, but for relative humidity.

Figure 15. NU-WRF/AMR equivalent potential temperature θ_e (shading) and wind vectors at 950 hPa at 120 h (valid at 0000 UTC 15 September) in the AMR simulation. Black contours show simulated radar reflectivity at 15, 30, and 45 dBZ and the red line indicates the 0.2 AOD threshold.

Figure 16. Area-averaged vertical profiles of (a) cloud (ice, shaded; liquid, contours) and (b) precipitation (snow plus graupel, shaded; rain, contours) from Ctrl between 0000 UTC 11 September and 0000 UTC 17 September. All cloud hydrometeors have the same unit, 0.001 g kg^{-1}. The areal average was for a 900x900 km^2 storm-centered box. Other panels show the differences of the area-averaged profiles from Ctrl for (c, d) Exp. AMR, (e, f) Exp. AM, and (g, h) Exp. AR.

Figure 17. Similar to Fig. 16, but for (a, b) Exp. AMR_SSO, (c, d) Exp. AMR_CO, (e, f) Exp. AMR_ABD, and (g, h) Exp. AMR_DO.

Experiment	Aerosol Impact
Ctrl	No Aerosol Coupling
AM	Microphysics Coupling Only
AR	Radiation Coupling Only
AMR	Microphysics/Radiation Coupling
AMR-ABD	AMR with all aerosol species but dust
AMR-CO	AMR with Carbon only
AMR-SSO	AMR with Sea Salt only
AMR-DO	AMR with Dust only

Table 1 List of all model experiments.

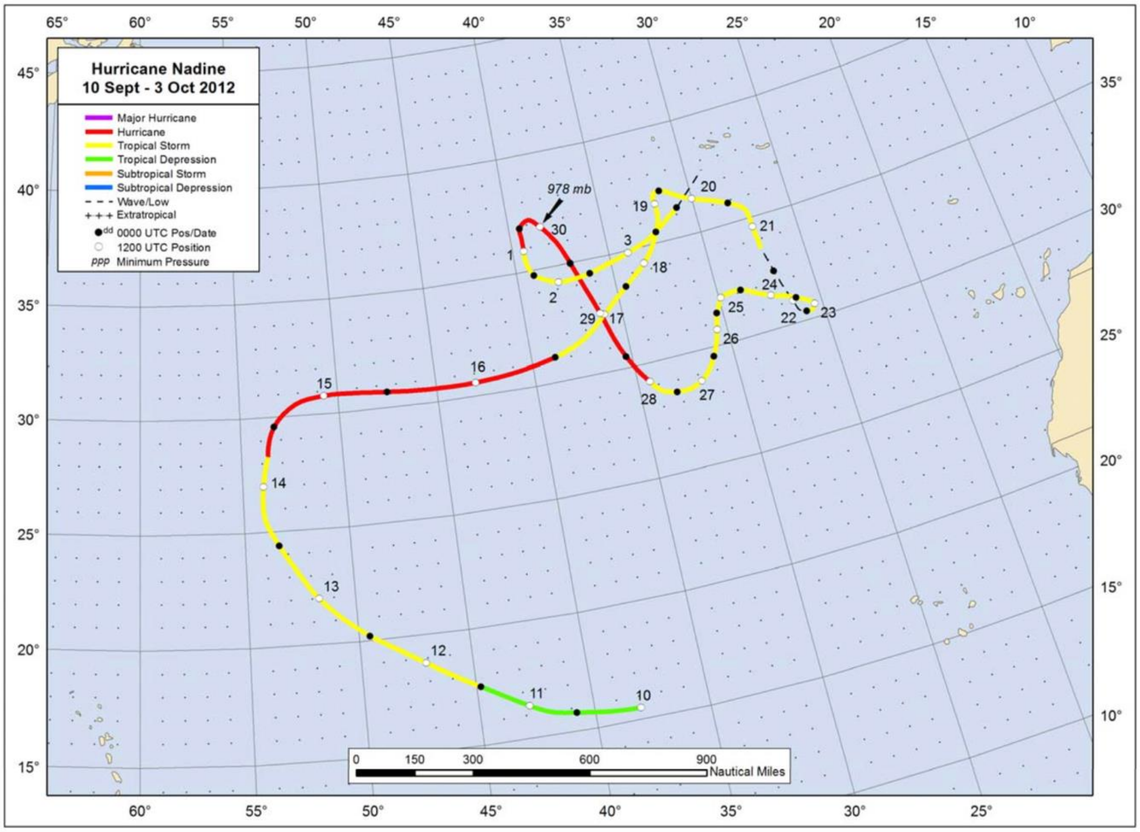

Figure 1. Best track of Hurricane Nadine (2012) adopted from the National Hurricane Center (NHC), https://www.nhc.noaa.gov/data/tcr/AL142012_Nadine.pdf.

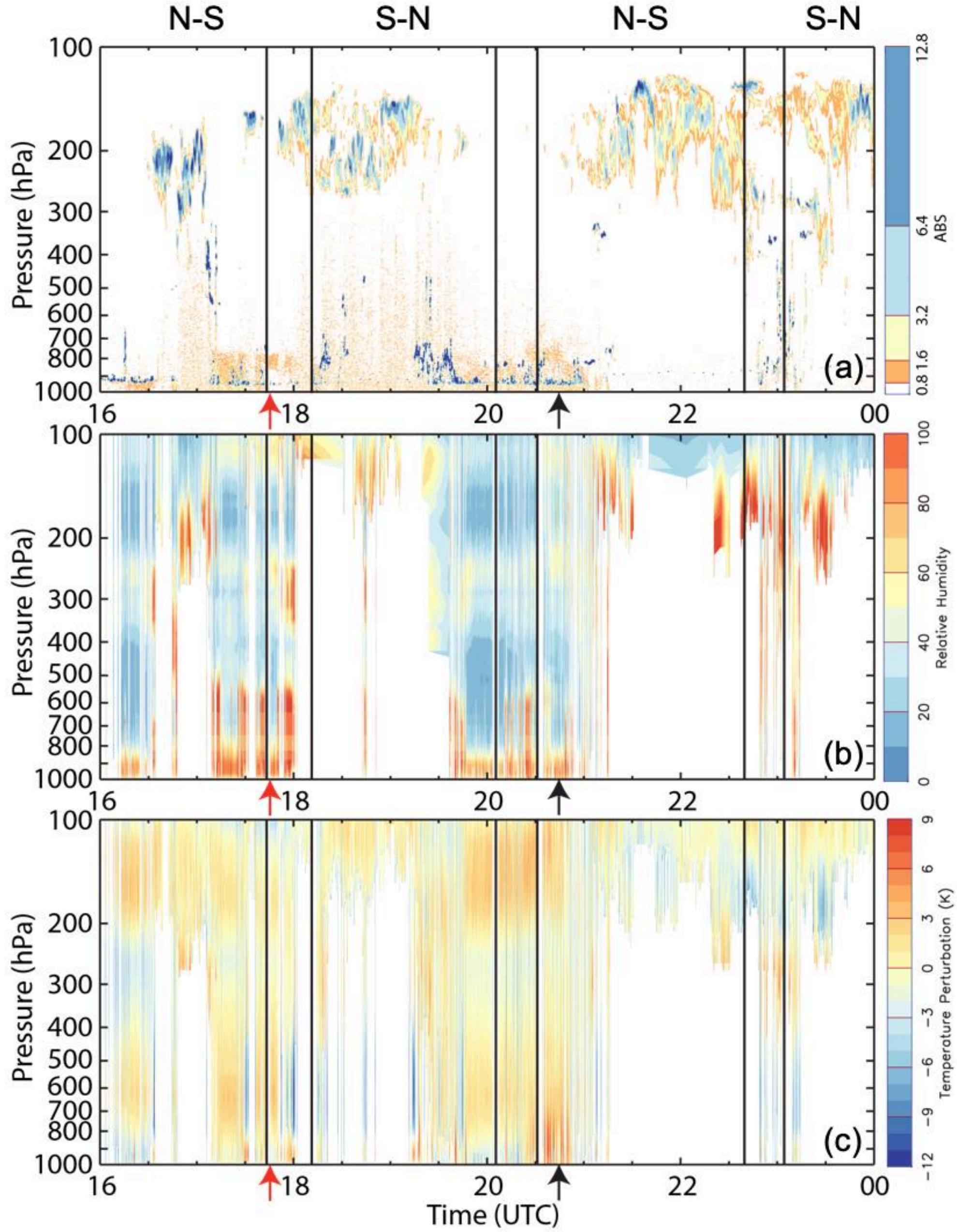

Figure 2. (a) CPL aerosol backscatter (×10^{-2} km^{-1} sr^{-1}) along the western portion of the Global Hawk flight path (red line in Fig. 9b) during the 11-12 September 2012 flight. S-HIS (b) relative humidity with respect to water and (c) temperature perturbation for the same flight segment. North-south flight legs are 10-12° latitude in length while the west-east legs are about 2° longitude in length. In (a), regions of weak backscatter beneath high clouds represents noise in the signal rather than particulate backscatter. Temperature perturbations are derived by removing the average temperature from 2000 UTC 11 September to 0600 UTC 12 September, similar to the approach used in Braun et al. (2016). Arrows indicate the times of dropsondes shown in Fig. 3, red for the 1746 UTC and black for the 2045 UTC 11 September dropsondes. In some locations, there is a reversal in the temperature anomalies below 400 hPa and much higher low-level relative humidity, suggesting possible retrieval biases caused by upper-level clouds. Three

sets of twin vertical lines indicate the times of aircraft turns to and from the north-south oriented flight legs.

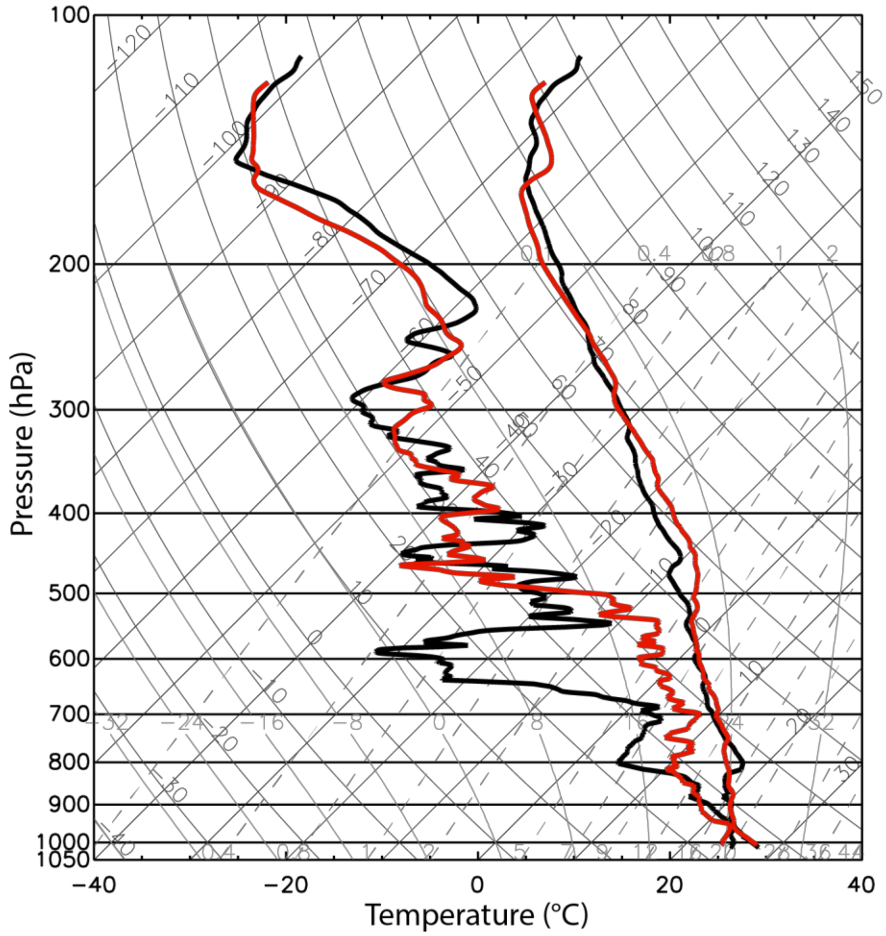

Figure 3. Skew-T log-p diagram showing the 1746 UTC (red) and 2045 UTC (black) dropsonde-derived temperature and dewpoint temperature profiles on 11 September. The 1746 UTC profile was released from the Global Hawk at 51.60°W, 15.43°, while the 2045 UTC dropsonde was released at 46.49°W, 24.24°N.

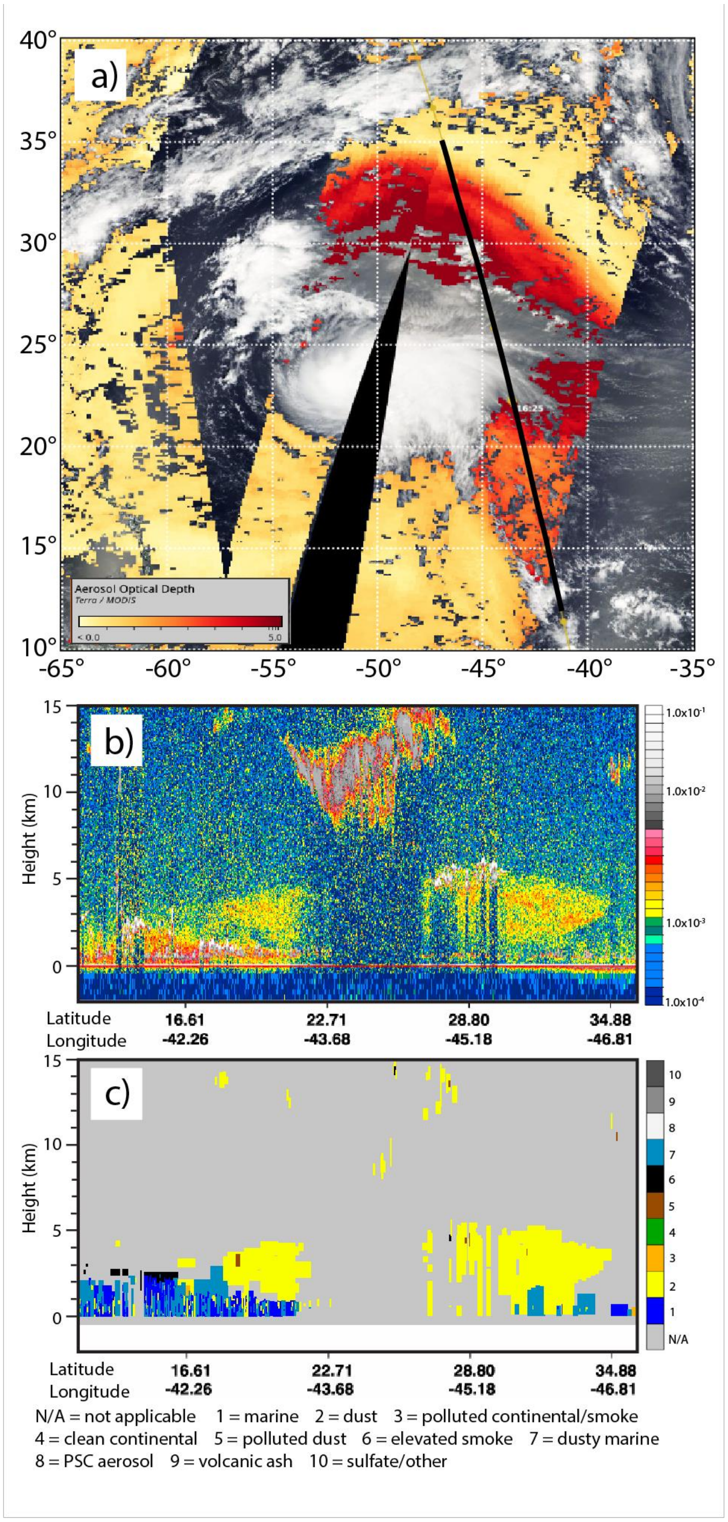

Figure 4. (a) MODIS aerosol optical depth and clouds for September 13, 2012. The location of a CALIPSO overpass is shown by the black line. Plot generated from NASA Worldview (https://worldview.earthdata.nasa.gov). The black line also represents the location of the cross-

sections shown in (b) CALIPSO 532-nm total attenuated backscatter and (c) aerosol subtype (bottom) at ~1628 UTC 13 September 2012. The figure was adapted from online CALIPSO browse images, version 4.10, at https://www.calipso.larc.nasa.gov/products/lidar/browse_images/production/.

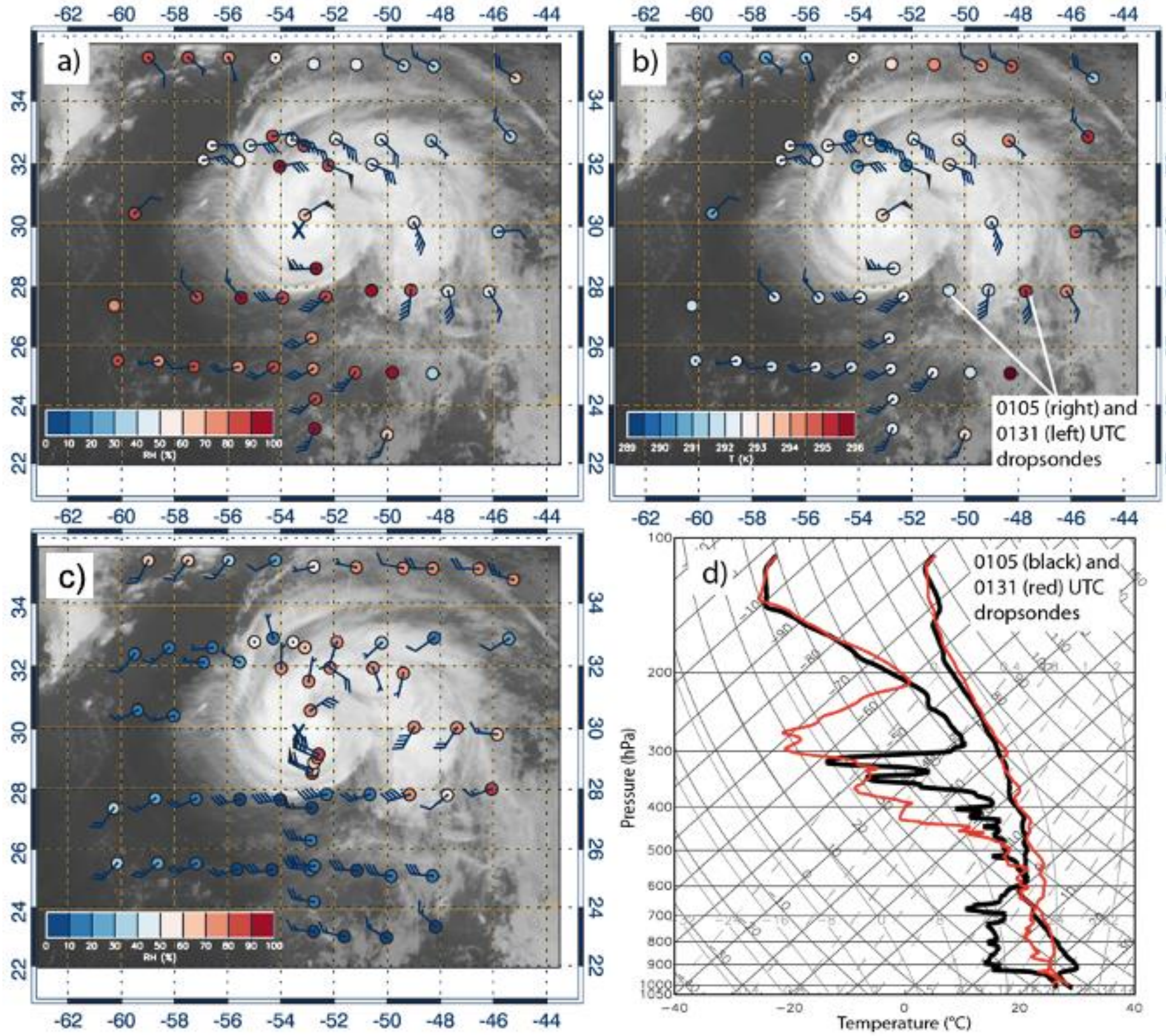

Figure 5. (a) Relative humidity (colored circles) and (b) temperature (colored circles), along with wind barbs (full barb, 5 m s^{-1}; half-barb, 2.5 m s^{-1}; flags, 25 m s^{-1}) at 875 hPa superimposed on the GOES infrared imagery at 0015 UTC 15 September 2012. (c) Same as (a), but for relative humidity at 400 hPa. Dropsonde locations account for dropsonde drift (i.e., uses the GPS-determined position at each height rather than the initial drop location or splashdown location) and storm motion, with positions adjusted to a reference time of 0000 UTC 15 September. (d) Dropsonde temperature and dewpoint temperature profiles at 0105 UTC 15 September (black) in the SAL air mass and 0131 UTC (red) in the non-SAL air mass to the east and west, respectively, of Nadine's outer rainband (see inset in panel b).

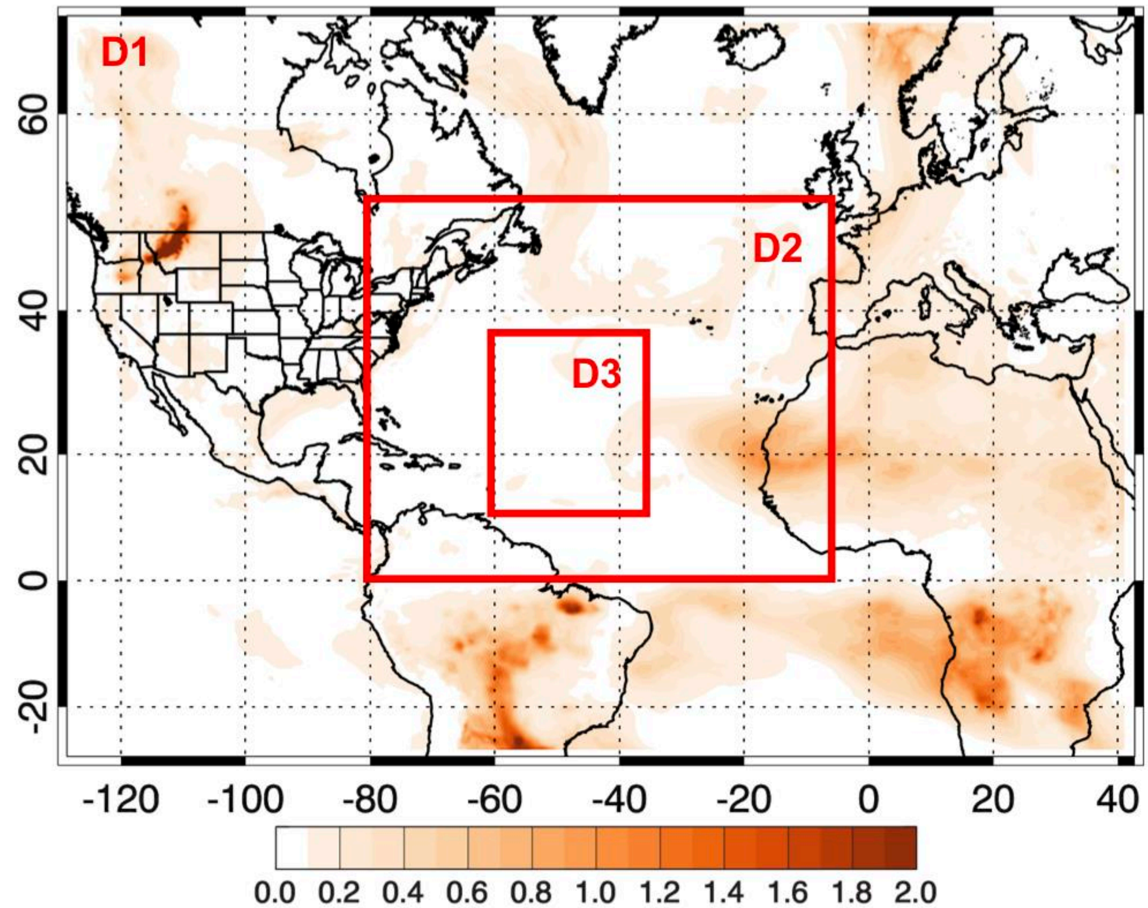

Figure 6. NU-WRF double-nested domains used for this study with horizontal grid spacings of 27, 9, and 3 km. The shading represents the analyzed AOD at the model initial time of 0000 UTC September 10, 2012.

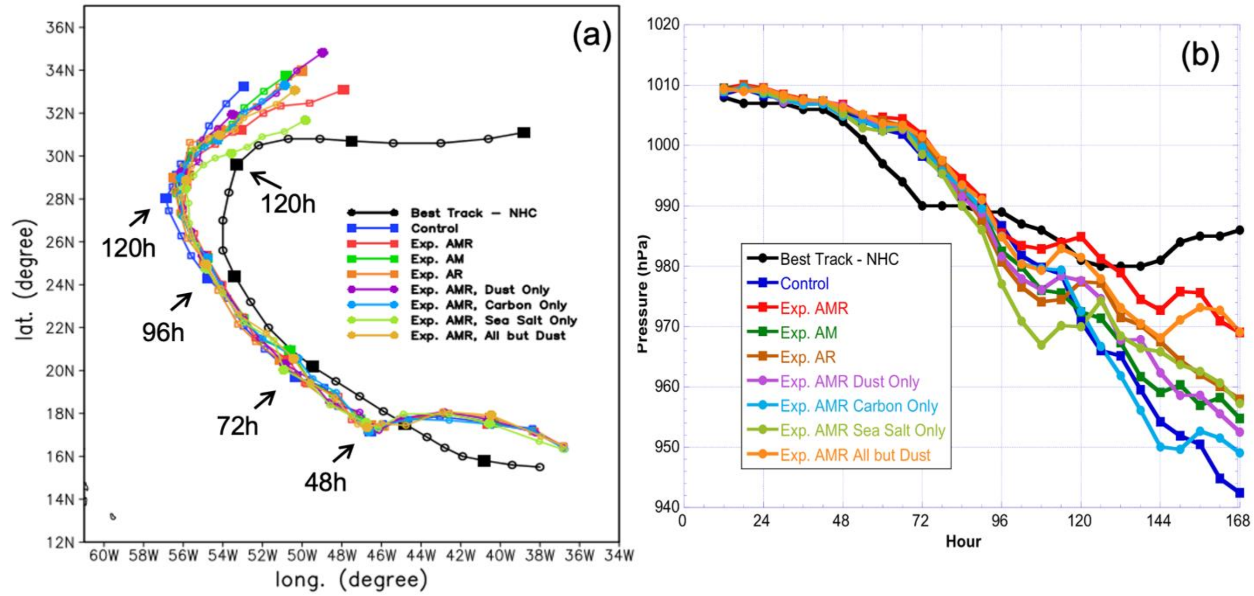

Figure 7. (a) Tracks and (b) minimum sea level pressures (MSLP) from the NHC best track and all NU-WRF experiment runs. Marks on all curves indicate a 6-h interval. The first mark in all curves represents the model time at 12h (1200 UTC 10 September 2012). The solid square mark on each curve represents the model time at every 24h.

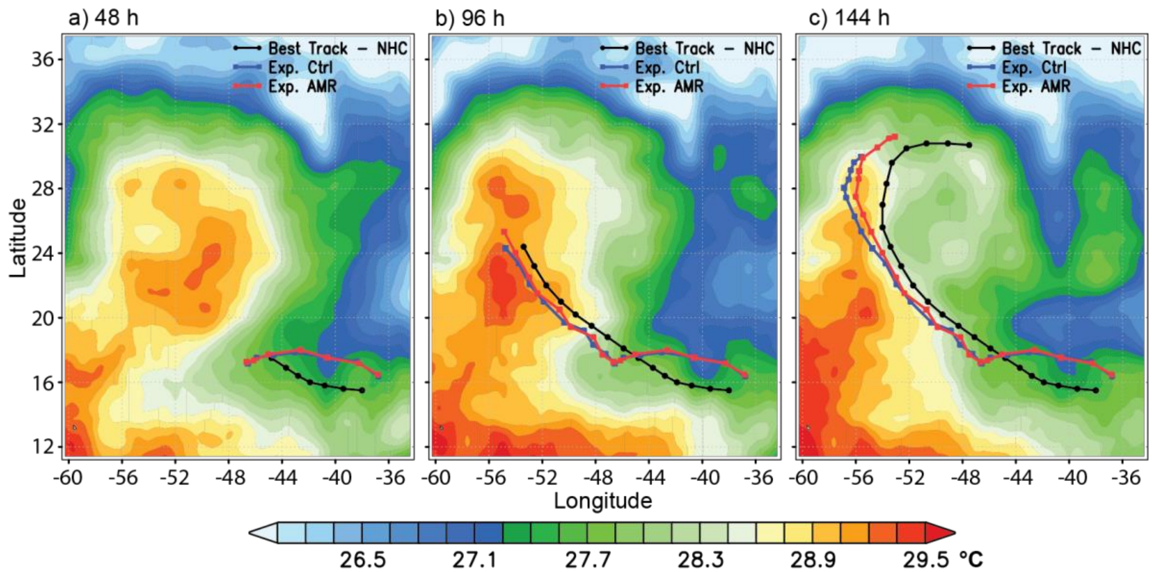

Figure 8. The ERA-Interim sea-surface temperature analysis every 48 h relative to the initial time of the simulations (0000 UTC 10 September). For reference, the plotted storm tracks are from the NHC best track (black line) and from the simulated tracks for Exps. Ctrl (blue line) and AMR (red line).

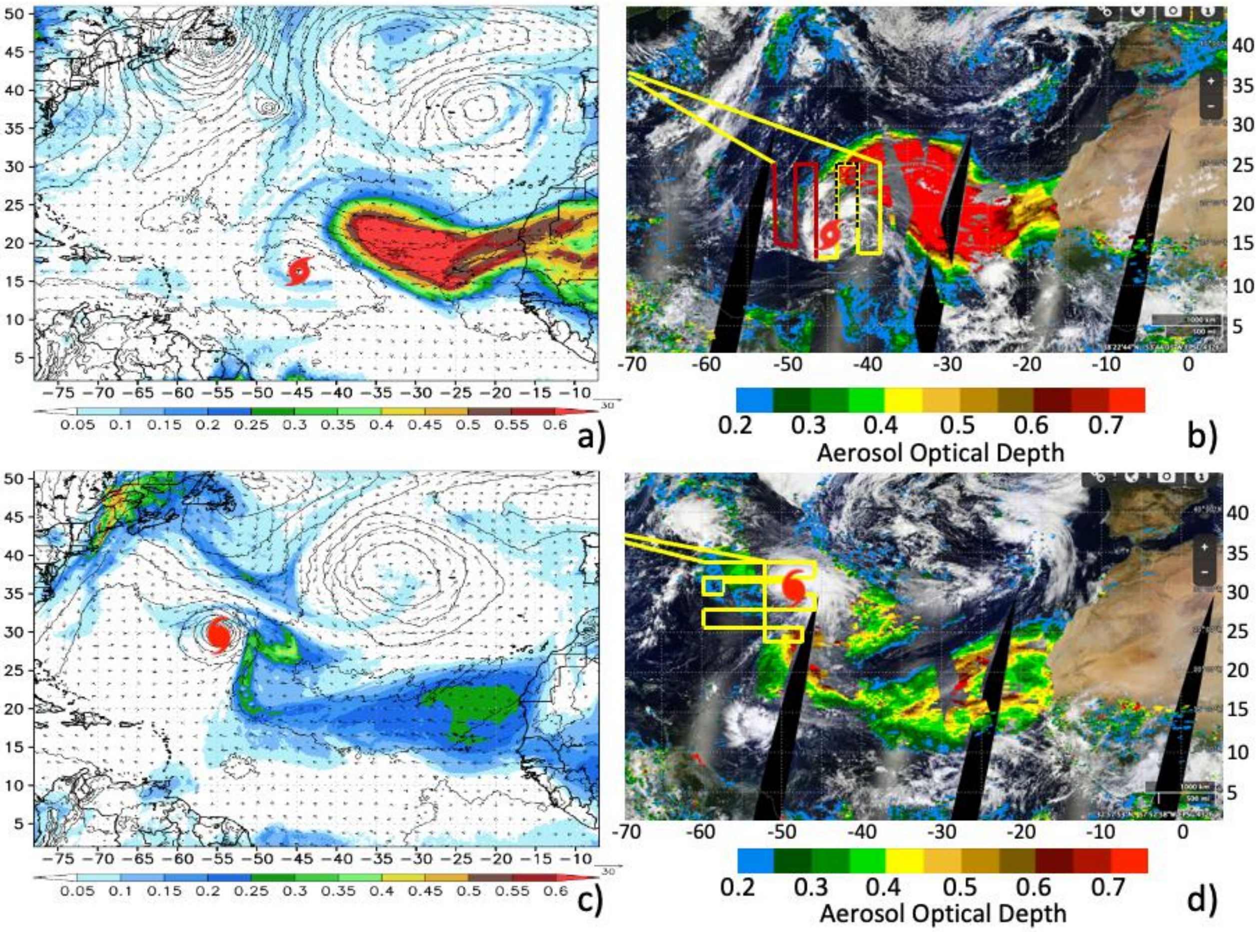

Figure 9. NU-WRF/AMR AOD from domain 2 at (a) 1200 UTC 11 and (c) 1200 UTC 15 September compared with daytime MODIS AOD on (b) 11 and (d) 15 September. Superimposed on the satellite image in (b) is the Global Hawk flight track for the 11-12 September flight, with red lines indicating the portion of the flight-track data shown in Fig. 2. Dashed lines indicate the data shown in Fig. 9 of B16. The Global Hawk flight track for the 14-15 September flight is shown in (d), with the flight pattern completed before the time of the image.

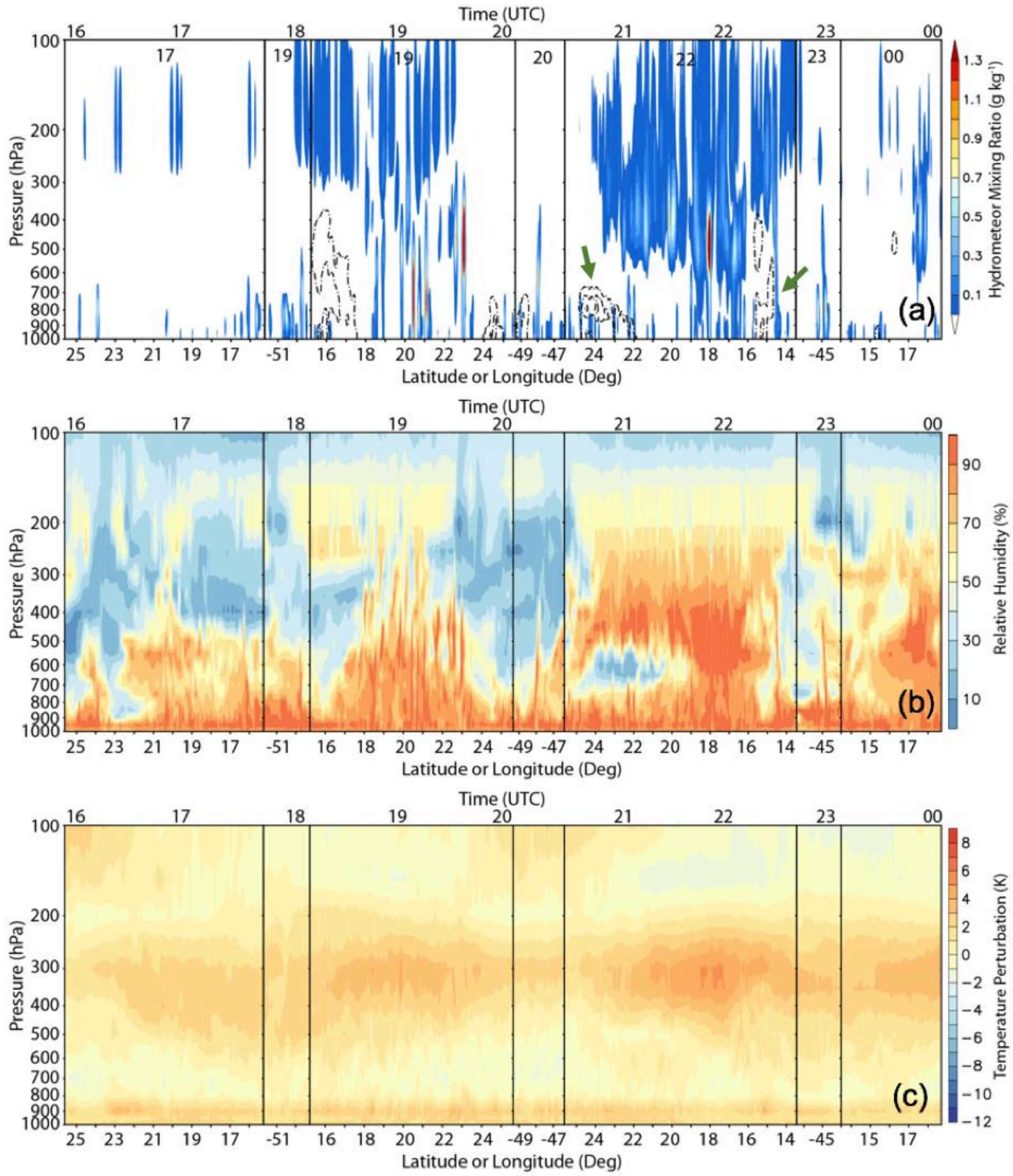

Figure 10. Similar to Fig. 2 except derived from Exp. AMR. However, (a) shows the total hydrometeor mixing ratio ($g\ kg^{-1}$, shading) from all cloud species while Fig. 2a is the CPL backscatter. Also in (a), dashed contours show dust mixing ratios at 10, 30 and 50 $\mu g\ kg^{-1}$. The row of numbers above each figure indicates the approximate UTC time on September 11 while the numbers just below the top axis in (a) indicates the model hour used to create the cross section. The numbers along the x-axis indcate the latitude (longitude) for the north-south (west-east) tracks. Green arrows in (a) indicate features discussed in the text.

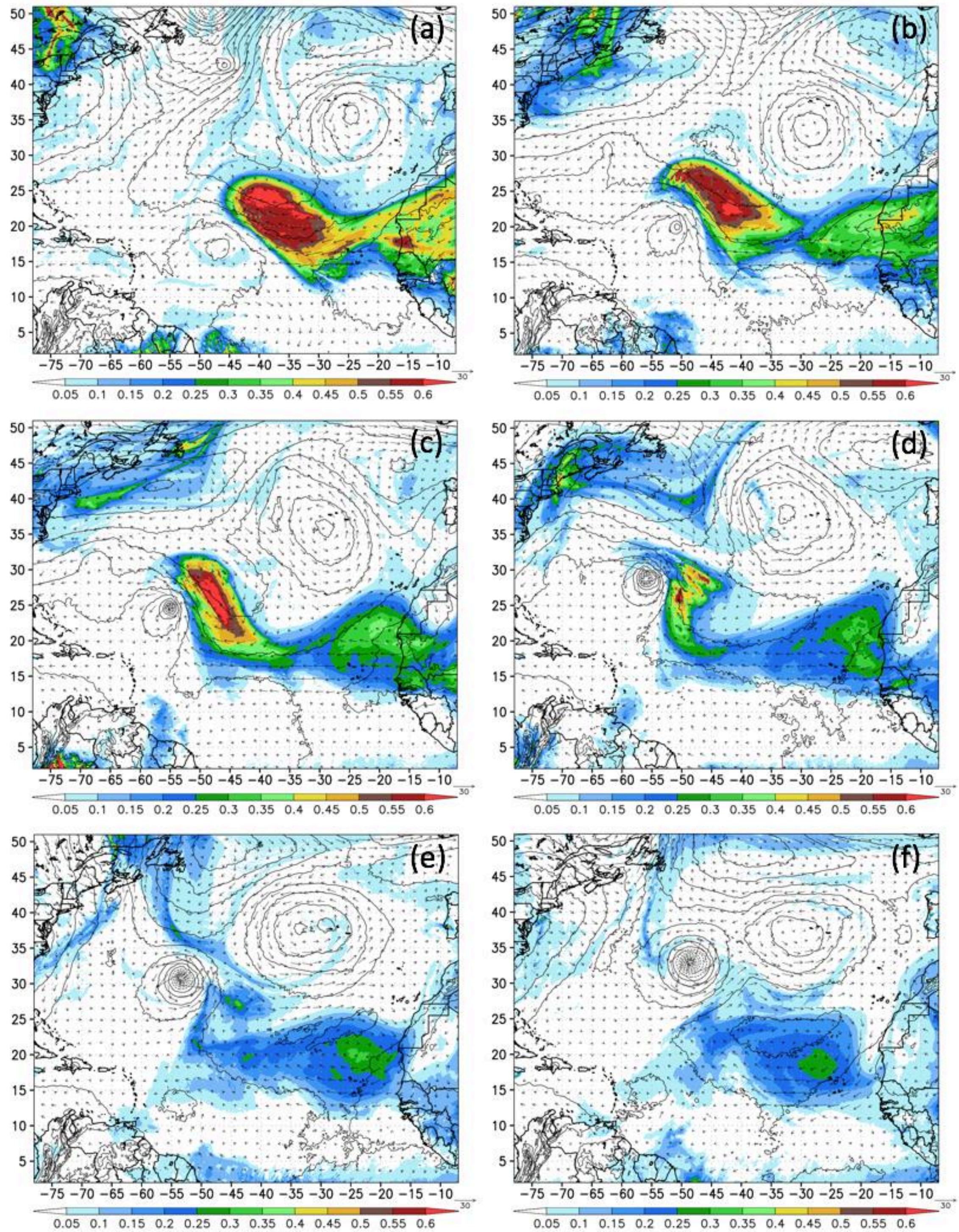

Figure 11. NU-WRF/AMR simulated AOD (shaded), mean sea-level pressure (hPa, contours) and 800-hPa wind (m s^{-1}, vectors) from domain 2 at a) 48 h, b) 72 h, c) 96 h, d) 120 h, e) 144 h, and f) 168 h valid at 0000 UTC of September 12, 13, 14, 15, 16, and 17.

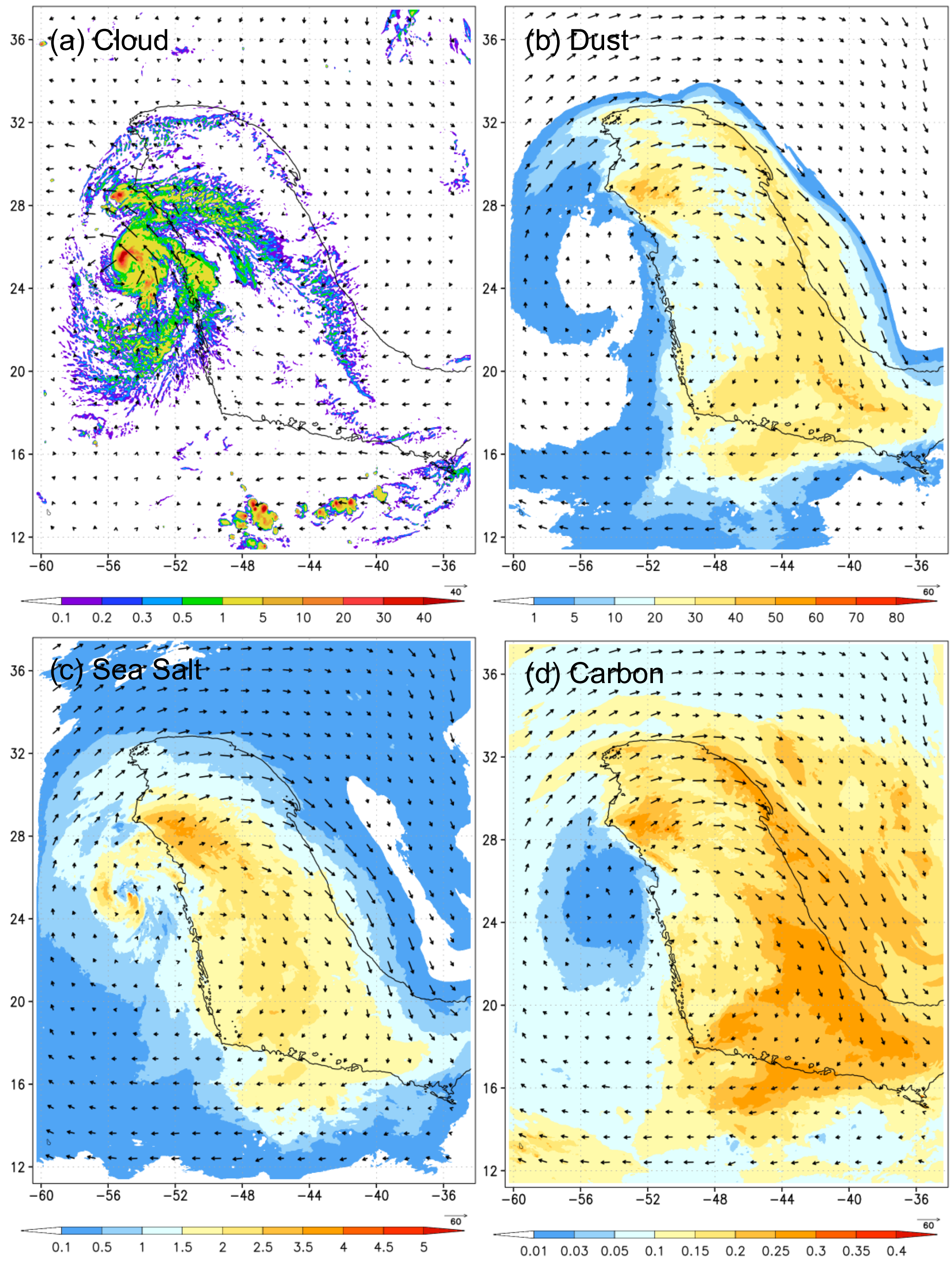

Figure 12. NU-WRF/AMR simulated horizontal distributions (shading) of 300-100 hPa layer-averaged (a) cloud (ice+snow+graupel) mixing ratio (0.01 g kg^{-1}), (b) dust mixing ratio (μg kg^{-1}), (c) sea salt mixing ratio (μg kg^{-1}), and (d) black and organic carbon mixing ratio (μg kg^{-1}) at 96h (valid at 0000UTC 14 September). The black contour shows the AOD=0.2 threshold. Vectors in (a) show 900-hPa winds, while in (b)-(d), vectors indicate 200-hPa winds, taken to be representative of the outflow layer.

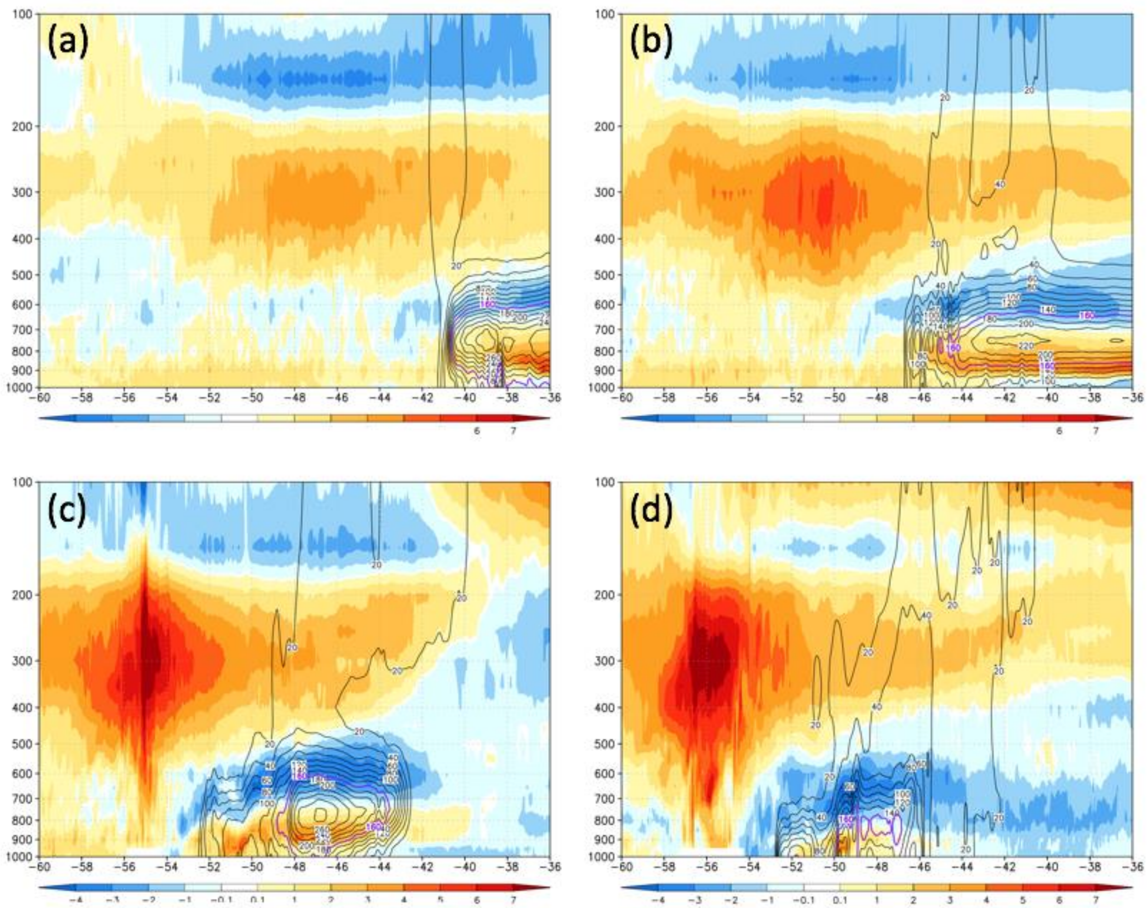

Figure 13. West to east cross sections through the storm core of the NU-WRF/AMR temperature perturbation (from the domain mean at 0 h, shaded) and dust (μg/kg-dry air, contours) at a) 48 h, b) 72 h, c) 96 h, and d) 120 h valid at 0000 UTC of September 12, 13, 14, and 15.

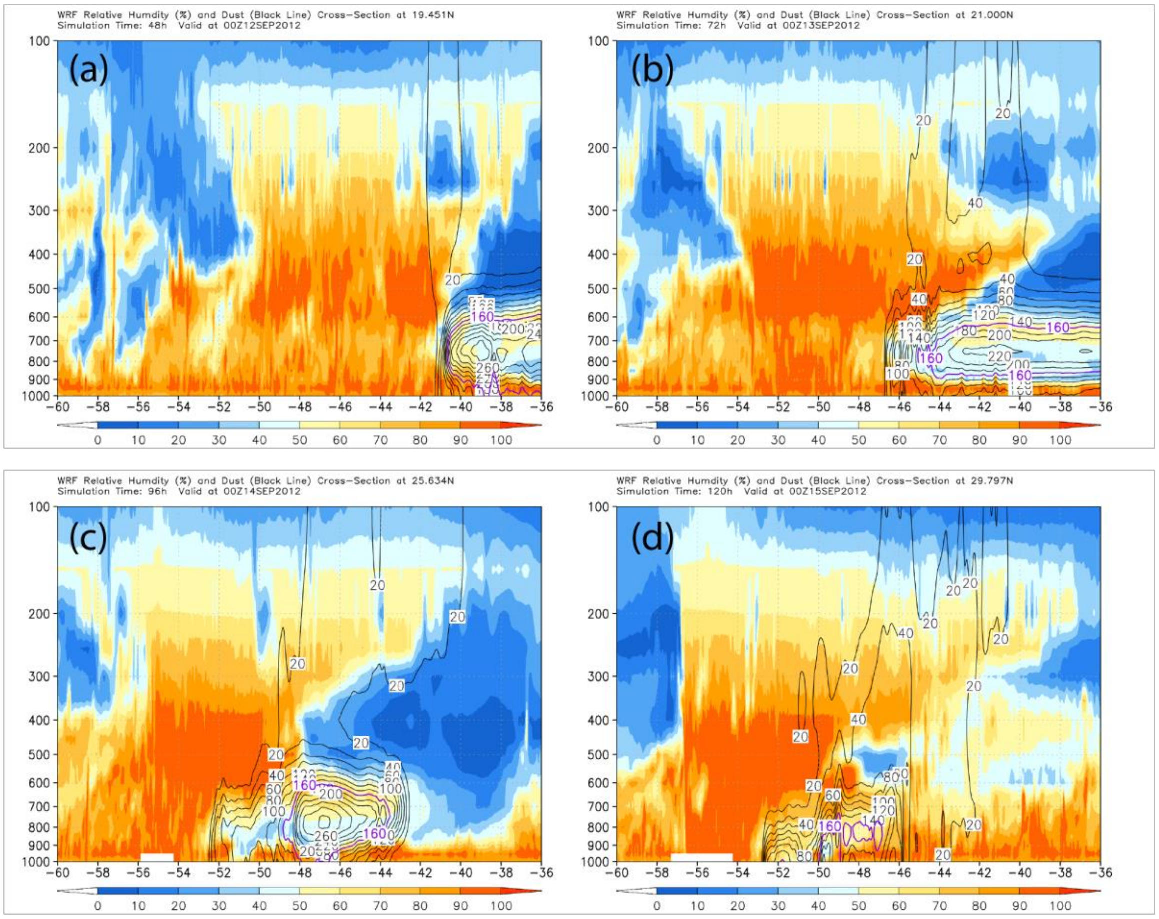

Figure 14. Same as Fig. 13, but for relative humidity.

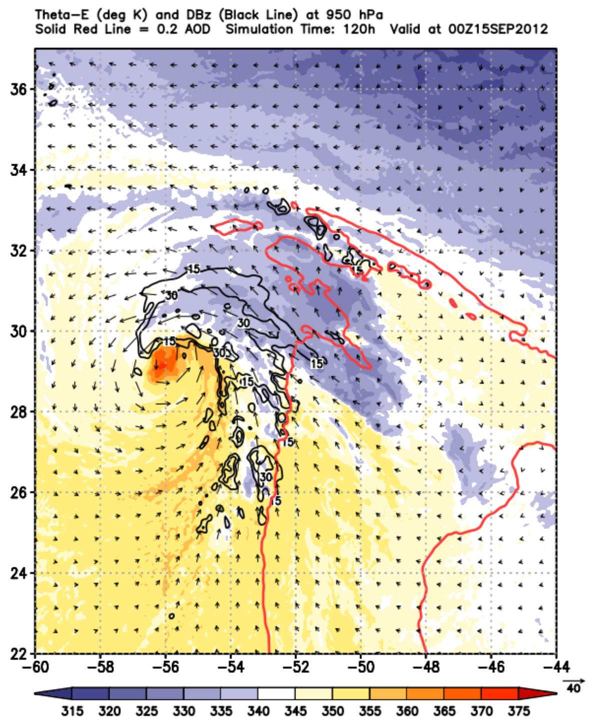

Figure 15. NU-WRF/AMR equivalent potential temperature θ_e (shading) and wind vectors at 950 hPa at 120 h (valid at 0000 UTC 15 September) in the AMR simulation. Black contours show simulated radar reflectivity at 15, 30, and 45 dBZ and the red line indicates the 0.2 AOD threshold.

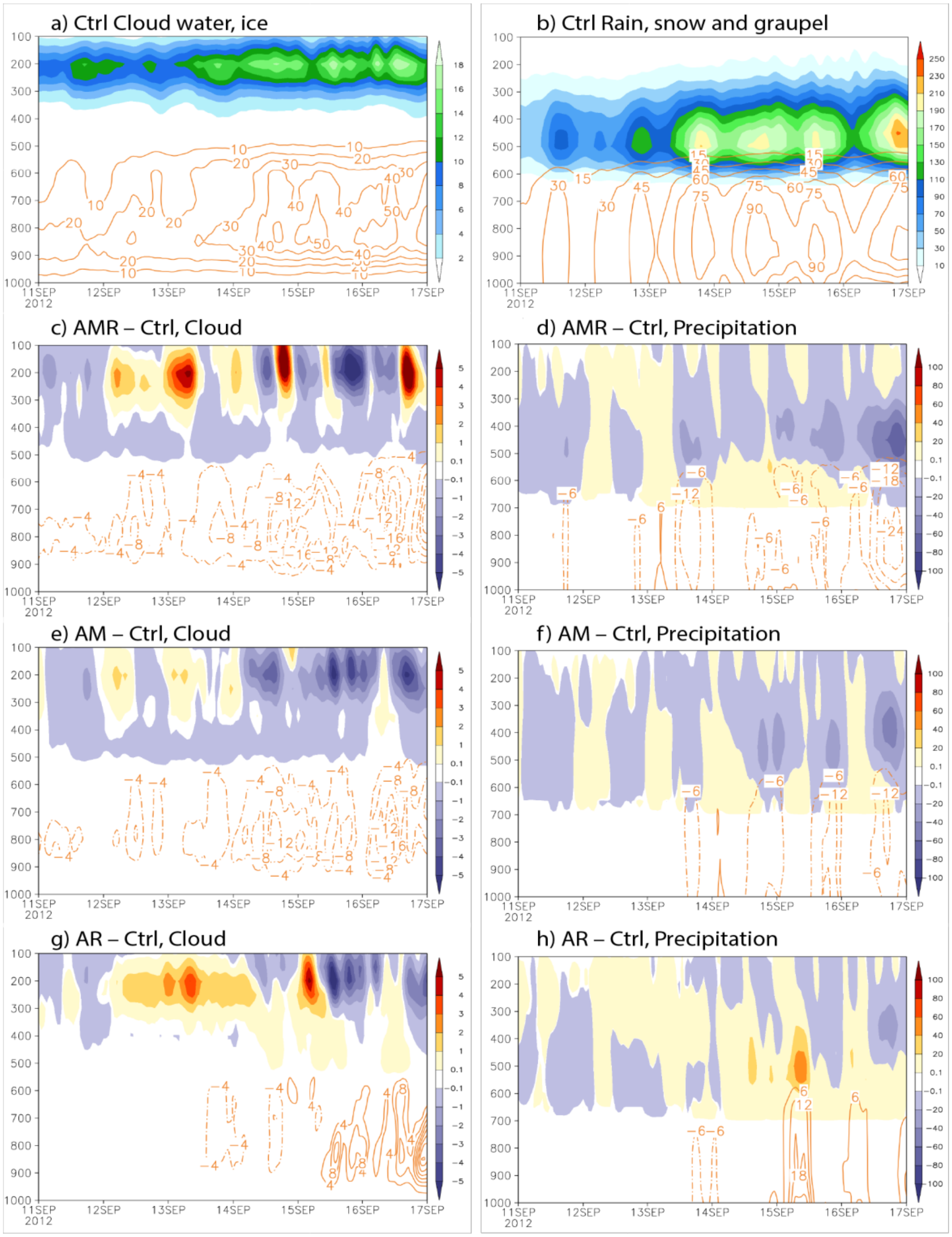

Figure 16. Evolution of Area-averaged vertical profiles of (a) cloud (ice, shaded; liquid, contours) and (b) precipitation (snow plus graupel, shaded; rain, contours) from Ctrl between 0000 UTC 11 September and 0000 UTC 17 September. All cloud hydrometeors have the same unit: 0.001 g kg^{-1}. The areal average was for a 900x900 km^2 storm-centered box. Other panels show the differences of the area-averaged profiles from Ctrl for (c, d) Exp. AMR, (e, f) Exp. AM, and (g, h) Exp. AR.

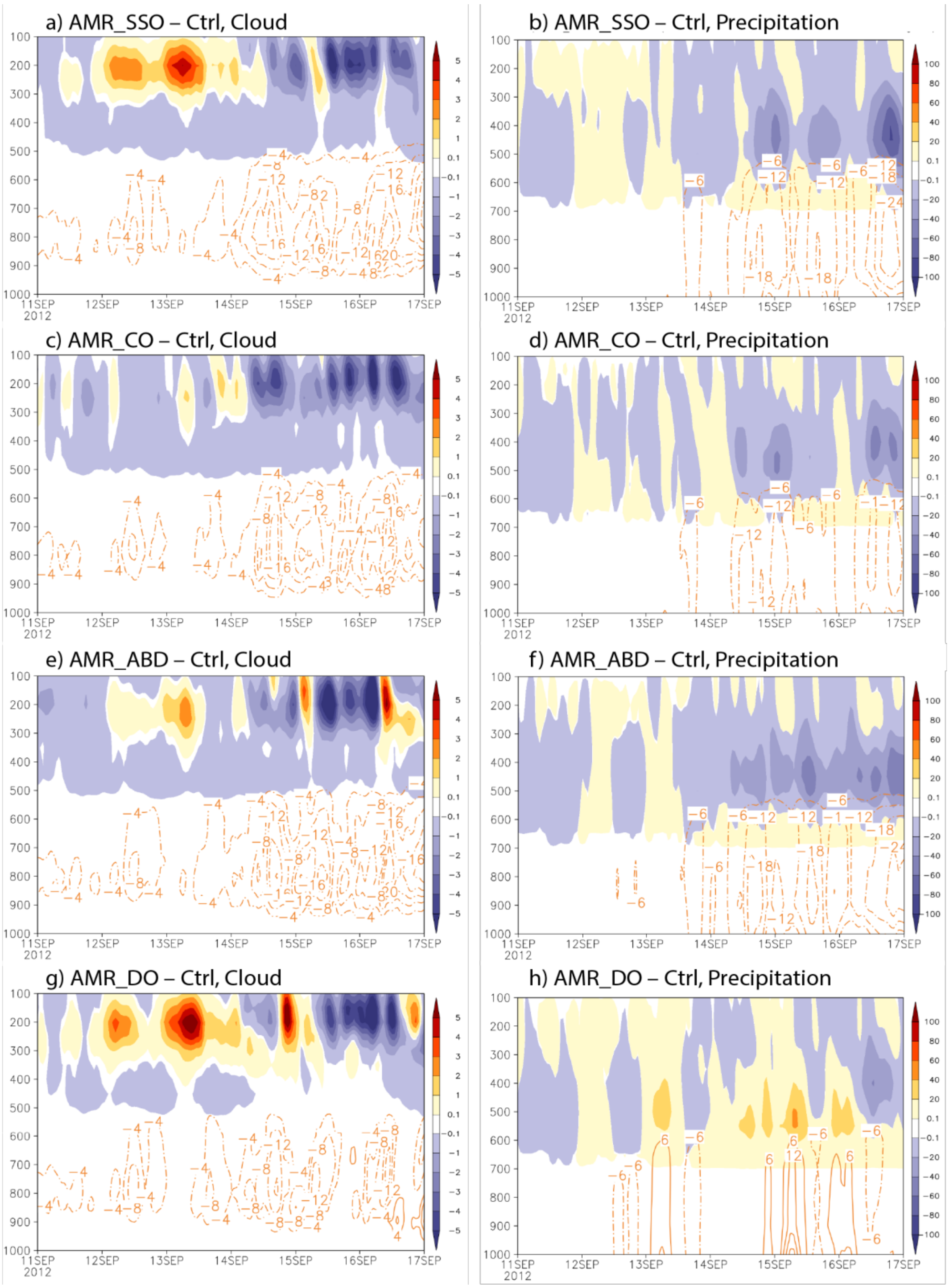

Figure 17. Similar to Fig. 16, but for (a, b) Exp. AMR_SSO, (c, d) Exp. AMR_CO, (e, f) Exp. AMR_ABD, and (g, h) Exp. AMR_DO.